Serrated Slat Cusp for High-lift Device Noise Reduction

Hasan Kamliya Jawahar,[1, a)] Syamir Alihan Showkat Ali,[2, b)] and Mahdi Azarpeyvand[1, c)]

[1)] *Department of Aerospace Engineering, University of Bristol, Bristol, BS8 1TR, UK.*

[2)] *Faculty of Mechanical Technology, University Malaysia Perlis (UniMAP), 02600, Arau, Perlis, Malaysia.*

(Dated: 8 December 2020)

Noise reduction capabilities of slat cusp serration were experimentally assessed and demonstrated for a 30P30N three-element high-lift airfoil fitted with two different types of serrated slat cusp. Aerodynamic characteristics were evaluated with the aid of surface pressure distribution and insignificant differences were found amongst all the tested configurations. The unsteady flow characteristics of the slat serrations were examined using near- and far-field measurements to gain a deeper understanding of the noise generation mechanism. Although increased surface pressure fluctuations were demonstrated by the slat serrations, a substantial reduction in the far-field noise was observed. The increase in the near-field energy levels was attributed to the non-propagating hydrodynamic energy field within the slat cove and the main-element, whereas the far-field noise reduction was attributed to the elimination of vortex shedding by the slat serration. Further reaffirmation of the observations and hypothesis were provided with higher-order spectral analysis and wavelet analysis.

Keywords: 30P30N, High-lift device, three-element airfoil, Slat noise, Serration, Aeroacoustics

[a)]Electronic mail: hasan.kj@bristol.ac.uk

[b)]Electronic mail: syamir@unimap.edu.my

[c)]Electronic mail: m.azarpeyvand@bristol.ac.uk

I. INTRODUCTION

Over the past decade, the boost in commercial air travel has stipulated the aircraft industry to produce efficient and quieter aircraft than the ones already in use. With the advent and use of high bypass engines for aircrafts, the noise generated by the engine has significantly been lowered, however, the airframe noise remains unaltered. During landing, the airframe noise is extensively dominated by high-lift devices and landing gears. In particular, High-lift devices like the slats are significant contributors to airframe noise and the resulting noise is both broadband and narrowband in nature. Considering overall airframe noise, various passive and active flow control methods are being explored to reduce noise, including methods like morphing structures[1–7], porous materials[8–11], surface treatments[12], serrations[13–15] and transverse jets[16,17]. Nonetheless, the noise generated by conventional slat and wing configurations continue to remain unresolved. It should be noted that the slat noise majorly comprises of broadband ($St_s = 0.5-1$), and tonal noise components ($St_s = 1-5$) and in addition to this, studies have also shown several discrete tones at mid-frequency range ($St_s = 1-5$)[18–30].

The aeroacoustic characteristics of slat noise are yet to be fully understood and are still of much interest to researchers. Slat noise reduction mechanisms[31] that have proven successful are slat cove cover[32], slat hook extensions[33], slat cove filler[34–36], slat gap filler[37], slat acoustic liners[38], slat hook tripping[39], slat hook serrations[40], and slat trailing with porous or brush extensions[41,42]. One of the most definite ways proven to reduce the broadband noise generated from the slat is by filling the recirculation area within the slat cove[34–36,43–51]. It is well established that the tonal peaks generated by the slat are a result of self-sustained acoustic feedback loop generated by the interaction between the unsteady shear layer from the slat cusp and its impingement on the lower surface of the slat[36]. Filling the slat cavity has shown to have eliminated this tonal noise and also the broadband noise from the shear layer impingement. At first, in an attempt to eliminate the unsteady recirculation region within the slat cove, Horne *et al.*[34] from NASA tested a solid slat cove filler (SCF) on a Boeing 777-200 semi span model in the NASA Ames 40 by 80 foot Wind Tunnel and to maintain attached flow on the slat lower surface, the slat cove filler profiles were derived from CFD analysis. The results proved that slat cove filler was effective in reducing broadband slat noise up to 4-5 dB (measured using a microphone phased array). However, no aerodynamic measurements were presented in the above study.

Streett *et al.*[43] investigated the noise and basic aerodynamics of the SCF setup using a trapezoidal wing swept model and demonstrated the noise reduction to be sensitive to the angle of attack and SCF modification, with a reduction of 3-5 dB over a wide bandwidth. In addition, comparatively better aerodynamic performance over angles of attack less than 20° with an earlier stall of 2 degrees was observed for the SCF. Imamura *et al.*[46] and Ura *et al.*[47] highlighted that the lift characteristics of the high-lift airfoil was sensitive to the SCF profile despite its noise reduction capabilities. The study involved two SCF profiles with a design point based on angle of attack, while the results confirmed a noise reduction of up to 5 dB for both profiles, the lift characteristics remained the same. Furthermore, Tao and Sun[51] successfully optimized SCF profiles to generate maximum lift at a fixed angle of attack whilst reducing noise. Moreover, a recent study by Kamliya *et al.*[36] reported detailed aerodynamic and aeroacoustic characteristics of slat cove fillers. The results indicated that the slat cove fillers do not adversely affect the aerodynamic performance of the wing. It was also highlighted that the characteristic vortex shedding peak in the slat noise was eliminated with the use of slat cove fillers along with a noise reduction of up to 10 dB in the narrowband region and up to 3 dB in the broadband region.

When considering slat serration there is a substantial lack in the available literature. However, a parametric study using seven different slat serrations with increasing serration wavelength was performed by Kopiev *et al.*[40]. Serration with smaller wavelengths was shown to be sufficient enough for noise reduction of up to 8 dB for the narrow-band peak. Aerodynamic performance remained unaffected by the serrated slat hook with a smaller wavelength. Moreover, the characteristic narrowband peaks were eliminated by the use of slat serrations. Additionally, the parametric study also showed that serration with larger wavelength increased broadband noise and slightly degraded aerodynamic performance.

Considering the substantial lack of studies in the literature, the current experimental study aims to present the basic aerodynamic performance and detailed aeroacoustic characteristics of the serrated slat. High-quality aeroacoustic measurements were acquired from the state of the art aeroacoustic facility at the University of Bristol. The results are presented in terms of static surface pressure measurement, lift characteristics, unsteady surface pressure measurements, and far-field noise measurements. A comprehensive analysis using correlation studies, higher spectral order analysis and wavelet transforms along with stochastic analysis was performed to understand the noise reduction mechanism of the serrated slat cusps.

II. EXPERIMENTAL SETUP

A. Airfoil and Wind Tunnel Setup

A 30P30N three-element high-lift airfoil was manufactured using a computer-aided numerically controlled machine with a retracted chord length of $c = 0.35$ m and a span length of $l = 0.53$ m. The geometrical parameters of the airfoil are detailed in Table I. The high-lift airfoil was designed with no brackets within the span of the test section to maintain two-dimensionality of the flow inside the slat cove and flap cove regions. A rigid purpose-built steel clamp was used to hold the three-elements together from the sides of the airfoil outside the test section. The slat was built with a spanwise slot to facilitate interchangeable slat leading-edge devices. The Cartesian coordinates $x-$, $y-$, and $z-axis$ corresponds to streamwise, crosswise and spanwise directions respectively. To induce turbulence in the slat shear layer, a zig-zag turbulator tape with a thickness of $h_t = 0.5$ mm and a width of $w_t = 3$ mm, with a turbulator angle of 70° was used at location $x/c = -0.055$ on the pressure side of the slat surface upstream from the slat cusp[20]. The airfoil was also equipped with 103 static pressure taps, placed along the mid-span of the airfoil for aerodynamic measurements. The tests were carried out for two different types of interchangeable serrated slat cusp configurations, detailed in Table II and shown in Fig. 2.

Aerodynamic measurements were performed in the low turbulence closed-circuit wind tunnel facility at the University of Bristol. It has an octagonal working area of 0.8 m × 0.6 m × 1 m and a contraction ratio of 12:1, with the capability of velocities up to 100 m/s and typical turbulence intensity levels as low as 0.05%. Furthermore, aeroacoustic measurements were carried out at the University of Bristol Aeroacoustic Facility (see Fig. 1). It is a closed-circuit open-jet anechoic wind tunnel with a nozzle exit of 0.5 m × 0.775 m and a contraction ratio of 8.4:1. The wind tunnel is capable of velocities up to 40 m/s with turbulence levels as low as 0.25%[52].

1. Unsteady Pressure Measurements Setup

The unsteady surface pressure within the slat cove region was measured using the FG-23329-P07 pressure transducers or remote sensors where pressure transducers could not be used due to space constraints. Five FG-23329-P07 pressure transducers with a diameter of 2.5 mm, a height of 2.5 mm and a sensing area of 0.8 mm were installed on the main-element of the wing (see Fig. 3a

TABLE I: Schematic and geometrical parameters of the 30P30N three-element high-lift airfoil in percentage of stowed airfoil chord, $c = 0.35$ m.

(a) Slat

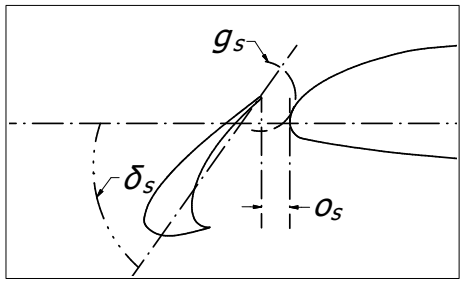

(b) Flap

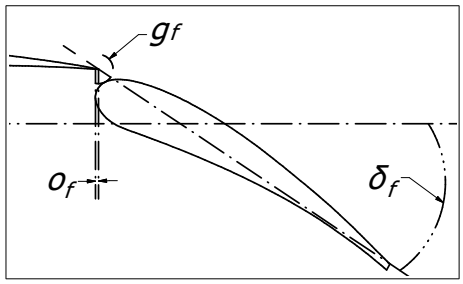

Slat chord	c_s	$0.15c$
Main-element chord	c_{me}	$0.83c$
Flap chord	c_f	$0.3c$
Slat deflection angle	δ_s	30°
Flap deflection angle	δ_f	30°
Slat gap	g_s	2.95%
Flap gap	g_f	1.27%
Slat overhang	o_s	−2.5%
Flap overhang	o_f	0.25%

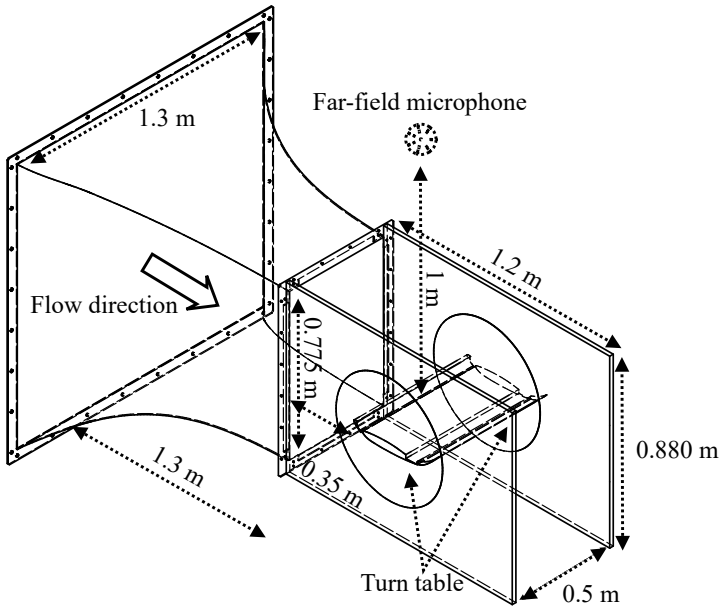

FIG. 1: Schematic of the 30P30N three-element high-lift airfoil set-up in the aeroacoustic wind tunnel.

and Table III). In order to reduce the measurement errors that arise due to the spatial integration

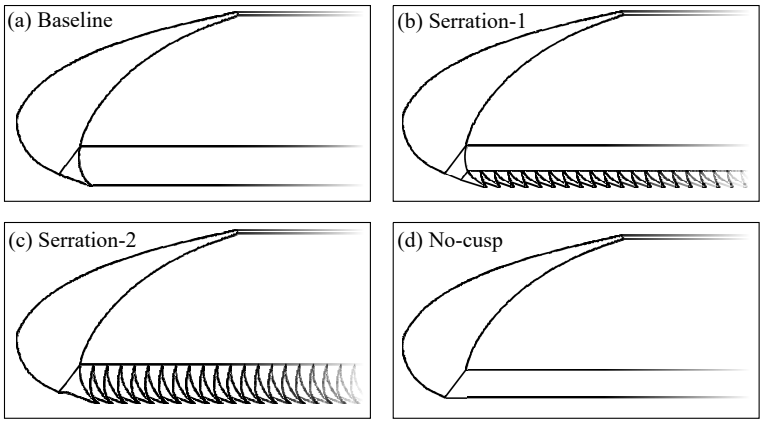

FIG. 2: Schematic of the different slat configurations tested in the present study: (a) Baseline, (b) Serration-1, (c) Serration-2, and (d) No-cusp.

TABLE II: Schematic of the slat cusp serration and its geometrical parameters tested in the present study.

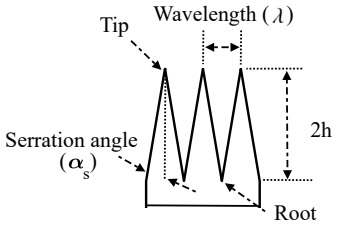

Configuration	$2h$	λ	λ/h	α_s
	(mm)	(mm)	-	(deg.)
Serration-1	3.8	3.12	1.64	67.7
Serration-2	6.4	3.12	0.975	76.3

of the signal, a surface fairing with a reduced sensing area of 0.4 mm was used (see Fig. 3b). The FG-23329-P07 is an electret condenser omnidirectional microphone with a flat frequency response between 100Hz-10kHz. It has a manufacture provided sensitivity of 22.4 mV/Pa in the flat region of the transducer response. For the current setup, in situ calibration was performed for the FG-transducers with a G.R.A.S 40PL piezoelectric microphone with a known manufacturer sensitivity and a flat frequency response up to 10 kHz with uncertainty level of $\pm$ 1 dB. It was found that the sensitivity for the FG-233329-P07 varied between 20.2 mV/Pa and 23.5 mV/Pa. In addition, four remote sensors made of Panasonic WM-61A miniature microphone were installed on the main-element and one on the slat of the wing, see Table III. As shown in Fig. 4, the remote sensors comprised of a brass pipe fitted in a designated slot on the surface of a metal base. The Panasonic WM-61A miniature microphone is placed in between a metal section and the metal base. Another drilled pinhole connecting to the surface of the brass pipe was aligned with the center of the microphone's pinhole. Furthermore, in order to eliminate the effect of standing waves, a flexible

tube extension of 2 m is connected to the other end of the brass pipe for anechoic termination. An in situ calibration was also performed for the remote sensor with the G.R.A.S 40PL piezoelectric
105 microphone that produced the transfer functions required to compensate for the high-frequency dissipation within the small tubes and the lag produced by the remote sensors extensions. For the current remote sensor setup, flat frequency response was found up to 6 kHz ($St_s = 10$). The unsteady surface pressure measurements using the FG-transducers and remote sensors were carried out for 120 seconds at a sampling frequency of $f = 2^{15}$ Hz.

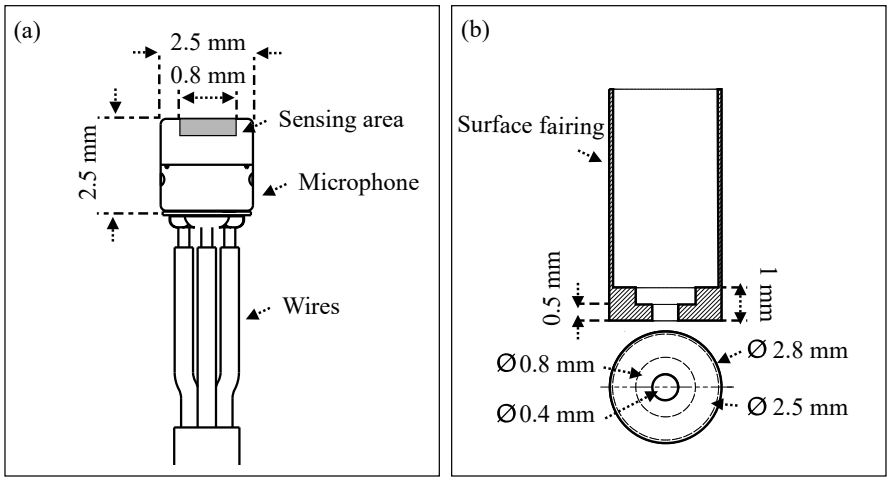

FIG. 3: (a) Schematic of the FG-23329-P07 pressure transducer and (b) schematic of the sectional view of the surface fairing for the pressure transducers.

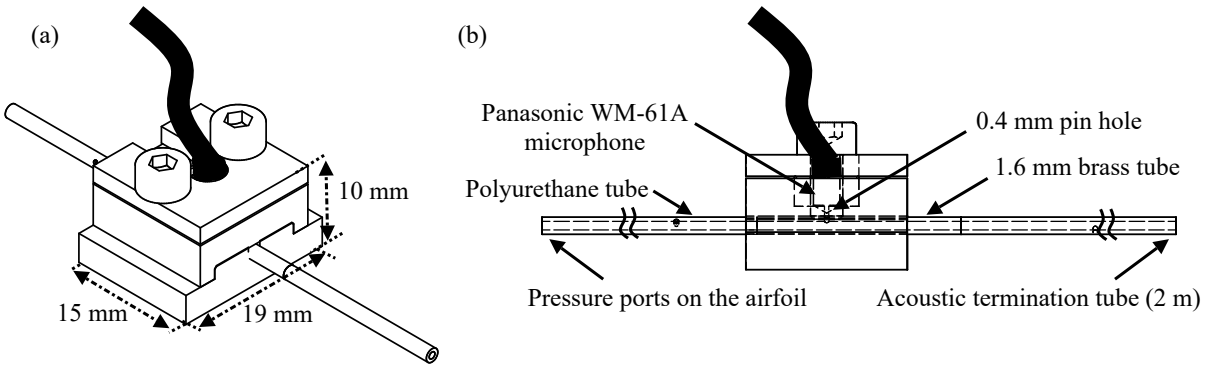

FIG. 4: (a) Schematic of the remote sensor configuration and (b) schematic of the sectional view of the remote sensor with description used in the present study.

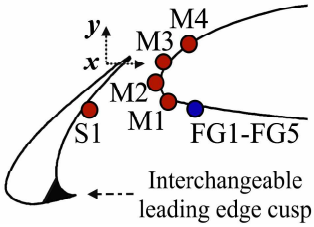

FIG. 5: Location of the remote unsteady pressure measurement sensors (red) and flush mounted surface pressure transducers (blue) on the slat and main-element of the 30P30N three-element high-lift airfoil.

TABLE III: Streamwise ($x - axis$) and spanwise ($z - axis$) unsteady pressure measurement locations on the slat and main-element for the 30P30N three-element high-lift airfoil.

No.	Type*	x (mm)	y (mm)	z (mm)
S1	RS	-6.918	-11.622	265
M1	RS	17.347	-10.019	265
M2	RS	15.126	-5.839	265
M3	RS	17.622	0	265
M4	RS	23.520	5.485	265
FG1	PT	22.414	-11.356	277
FG2	PT	22.414	-11.356	280.6
FG3	PT	22.414	-11.356	288.4
FG4	PT	22.414	-11.356	301.4
FG5	PT	22.414	-11.356	319.6
*RS - Remote sensor, PT - Pressure transducer				

2. Acoustic measurements and instrumentation

The experimental setup of the 30P30N three-element high-lift airfoil installed in the aeroacoustic facility is shown in Fig. 1. The far-field noise measurements were carried out using a Panasonic WM-61A electret microphone placed at a distance of 1 m and 90° away from the slat trailing edge. The far-field microphone has a flat frequency response at frequencies from 50 Hz to 10 kHz, with a dynamic range of more than 62 dB. The diameter of the exposed microphone diaphragm of the WM-61A microphones is 2 mm. The far-field noise data were captured for $t = 120$ s at a sampling frequency of $f = 2^{15}$ Hz. The acoustic data were recorded at a flow velocity of 30 m/s corresponding to a chord-based Reynolds number of $Re_c = 7.0 \times 10^5$. The power spectrum results were obtained using the power spectral density (PSD) of the pressure signals with Hanning window and the

acquired data were averaged for 220 times to yield a frequency resolution of $\Delta f = 2$ Hz. The sound pressure level (SPL) spectrum can then be calculated from $SPL = 20 \cdot log_{10}\ (p_{rms}/p_{ref})$, where p_{rms} is the root-mean-square of the acoustic pressure and $p_{ref} = 20\ \mu$Pa is the reference pressure. The sound pressure level of the acoustic pressure signal is corrected to a reference distance of 1 m.

III. RESULTS AND DISCUSSIONS

A. Test Conditions

It is of fundamental importance to assess and understand the aerodynamic behavior of high-lift devices for any modifications made to the slat. A quantitative comparison of the pressure coefficient for the Baseline, Serration-1, and Serration-2 configurations with existing data are presented in Fig. 6. The pressure coefficient distribution over the 30P30N three-element high-lift airfoil with and without the slat cusp serrations at a chord-based Reynolds number of $Re_c = 1.2 \times 10^6$ at the angle of attack $\alpha = 10^\circ$ are compared for validation purpose with published results available from Li *et al.*[27] at a chord-based Reynolds number of $Re_c = 1.71 \times 10^6$ at the angle of attack $\alpha = 8^\circ$. The surface pressure measurement for the high-lift configuration is highly dependent on the type of wind tunnel and the angle of attack[36,53]. Li *et al.*[27] demonstrated that the pressure coefficient distribution and the flow-field of a 30P30N three-element high-lift airfoil tested in a closed hard-wall wind tunnel were similar to the ideal free flight conditions unlike the results obtained from an open test section wind tunnel. The surface pressure coefficient results (C_p) of the Baseline, Serration-1, and Serration-2 configurations shown in Fig. 6 validate well with the open test section wind tunnel results from Li *et al.*[27]. This shows the validity of the airfoil used in the study and that the aerodynamic results presented in this study shall not be compared to that of the ideal free-flight conditions, due to the significant effects of the flow deflection and the sidewall interference[36].

B. Aerodynamic characteristics

The close-up view of the pressure coefficient distributions C_p around the slat and flap region of the 30P30N three-element high-lift airfoil for the Baseline, Serration-1, and Serration-2 cases at a chord-based Reynolds number of $Re_c = 1.2 \times 10^6$ at the angle of attack $\alpha = 10^\circ$ are presented in Fig. 7. Slat serrations generates insignificant changes in the pressure coefficient distribution over the

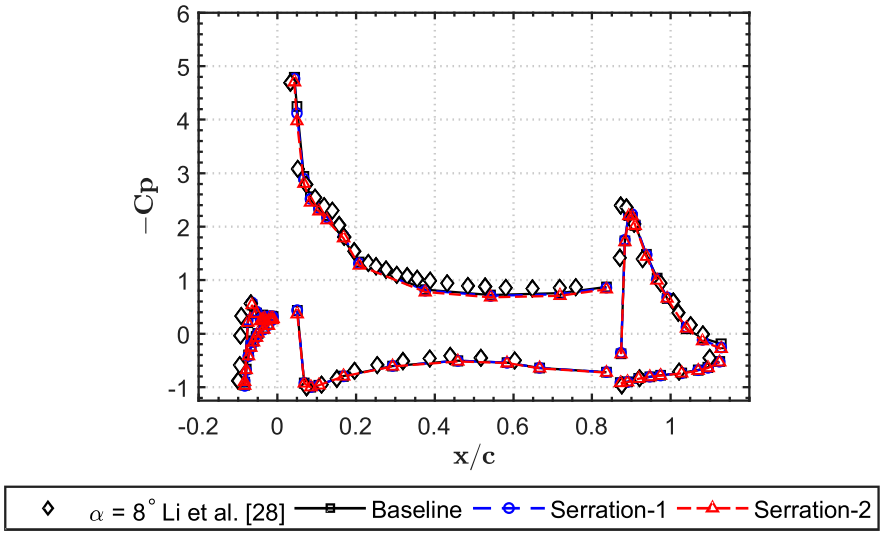

FIG. 6: Pressure coefficient distribution and validation over the 30P30N three-element high-lift airfoil with and without slat serrations for a free-stream velocity of $U_\infty = 50$ m/s, $Re_c = 1.2 \times 10^6$ at angle of attack $\alpha = 10°$.

slat and flap region for the tested Reynolds number compared to the Baseline case. Additionally, the C_p remains almost unchanged amongst all the three configurations over the main-element, as seen in Fig. 6. The lift coefficient (C_L) was calculated by applying the trapezoidal integration rule to the pressure data obtained from 103 pressure taps distributed over the three element of the 30P30N high-lift airfoil. Figure 8 shows the $C_L - \alpha$ curve for the Baseline, Serration-1 and Serration-2 configurations at a chord-based Reynolds number of $Re_c = 1.2 \times 10^6$. Measurements were performed for angles of attack ranging from $\alpha = 1°$ to $15°$ with an increment of $1°$. The lift coefficient (C_L) shows negligible difference amongst the cases for all the presented angles, of attack besides a negligible variation at angles of attack $\alpha = 1°, 4°$ and $5°$.

As shown in previous studies[27,36,53], it is a common practice to compare aerodynamic characteristics between two experimental or computational setup to establish the flow condition for high-lift devices. Figure 9 shows the pressure coefficient distribution over the slat region of the 30P30N Baseline configuration at the geometrical angle of attack $\alpha = 14°$ in the open-jet aeroacoustic wind tunnel from the present study compared to the aerodynamic angle of attack $\alpha = 5.5°$ from Murayama *et al.*[22] in a closed test section wind tunnel. The C_p results around the slat region at $\alpha = 14°$ were observed to correspond well with those of the $\alpha = 5.5°$ at free flight conditions reported by Murayama *et al.*[22]. It should be noted that all the following aeroacoustic results are

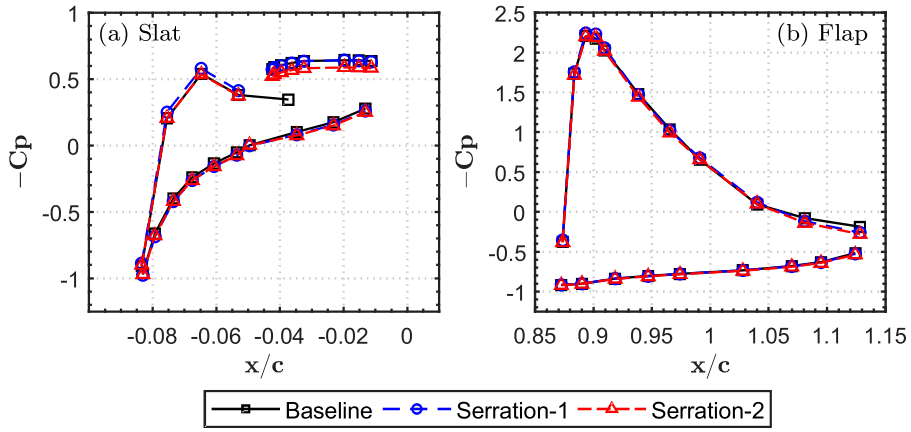

FIG. 7: Pressure coefficient distribution over 30P30N three-element high-lift airfoil around the (a) slat, and (b) flap region for a free-stream velocity of $U_\infty = 50$ m/s, $Re_c = 1.2 \times 10^6$ at angle of attack $\alpha = 10°$.

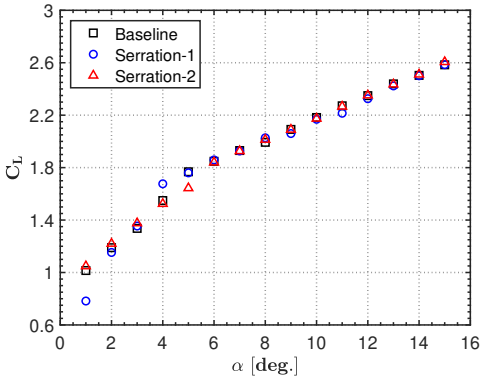

FIG. 8: Lift coefficient calculated using trapezoidal integration of the C_p distribution for the 30P30N three-element high-lift airfoil with serrations at a chord-based Reynolds number $Re_c = 1.2 \times 10^6$ ($U_\infty = 50$ m/s).

presented for the geometric angles of attack $\alpha = 14°$ and $18°$ in the open-jet aeroacoustic wind tunnel.

C. Far-field spectral levels

Far-field noise measurements were carried for the Baseline, Serration-1, and Serration-2 configurations. For the sake of comparison, results are also provided for a configuration without the slat cusp (No-Cusp). Figure 10 shows the sound pressure level measured from a far-field microphone at

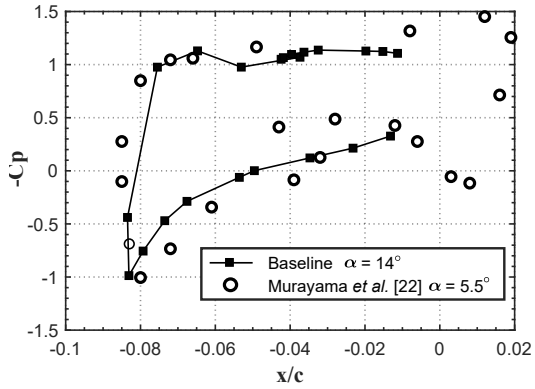

FIG. 9: Pressure distribution around the slat for the tested 30P30N Baseline configuration at geometrical angle of attack $\alpha = 14°$ in open jet configuration compared to the aerodynamic angle of attack $\alpha = 5.5°$ from Murayama *et al.*[22] in a closed test section.

90° and 1 m away from the slat trailing edge at angles of attack $\alpha = 14°$ and 18°, for a free-stream velocity of $U_\infty = 30$ m/s, corresponding to a chord-based Reynolds number of $Re_c = 7.0 \times 10^5$. The sound pressure levels (SPL) are presented in terms of slat based Strouhal number ($St_s = f \times c_s/U_\infty$). The SPL for the Baseline and Serration-1 configuration exhibits characteristic discrete narrowband peaks particularly at $St_s \approx 1.6$, typically found in high-lift devices. Interestingly, the far-field SPL of the Serration-2 and No-Cusp configurations do not demonstrate this tonal behavior at angle of attack $\alpha = 14°$. However, at $\alpha = 18°$, the No-Cusp configuration shows a narrowband peak with reduced energy at $St_s = 1.32$. Furthermore, at the angle of attack $\alpha = 14°$, the Serration-1 configuration clearly shows a reduction in noise levels at $St_s \approx 1.6$ but an increase at the angle of attack $\alpha = 18°$ at $St_s \approx 1.6$. Evidently, a slight shift in the peak Strouhal number to $St_s = 1.5$ (i.e. shift to a lower St_s number) is observed in the case of the Serration-1 compared to that of the narrowband peak seen at $St_s = 1.6$ for the Baseline configuration. Particularly, for Serration-2 at angles of attack $\alpha = 14°$ and 18°, significant noise reduction at the fundamental peak ($St_s = 1.6$) compared to that of the Baseline and Serration-1 cases are observed. Moreover, the SPL increases at low to mid-frequency range ($St_s < 2$) for the Serration-1, Serration-2, and No-Cusp configurations, and remain the same at high frequencies ($St_s > 2$) for both the angles of attack, $\alpha = 14°$ and 18°. However, at the spectral hump $St_s = 0.88$, all the slat modifications show noise reduction, with Serration-1 showing a reduction of up to 3 dB, and Serration-2 as well as No-Cusp configurations showing a reduction of up to 5 dB.

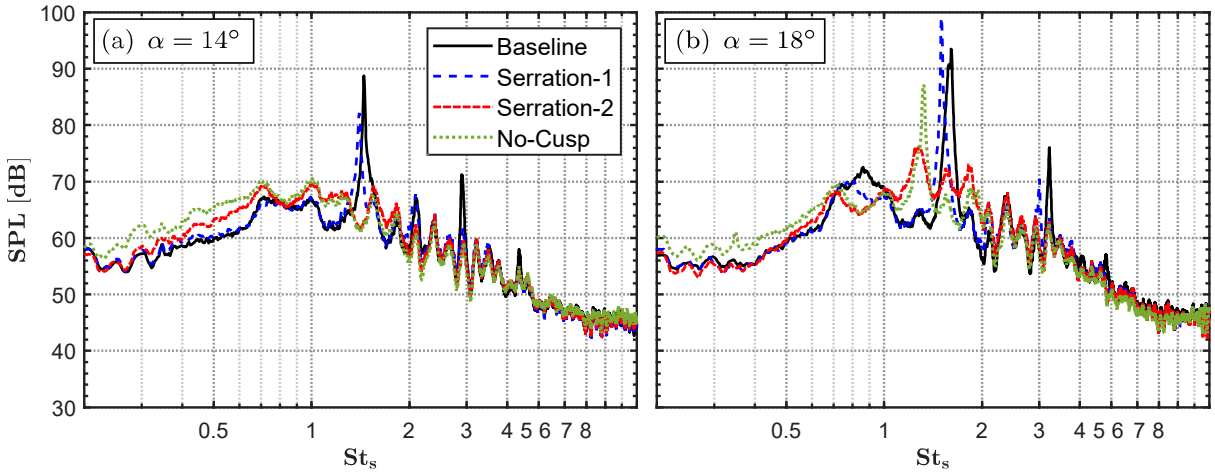

FIG. 10: Far-field noise spectra for microphone at 90° and 1 m away from the slat trailing edge: (a) $\alpha = 14°$ and (b) $\alpha = 18°$.

TABLE IV: Overall sound pressure level calculated from the far-field microphones at 90° and 1 m away from the slat trailing edge.

	OASPL [dB]	
Cases	$\alpha = 14°$	$\alpha = 18°$
Baseline	94.95	101.49
Serration-1	91.95	102.97
Serration-2	90.59	93.72
No-Cusp	90.63	95.53

To further improve our understanding of the differences in noise levels between the slat configurations, an estimation of the overall sound pressure level (OASPL) for the far-field microphone 90° and 1 m away from the slat trailing edge is presented in Table IV. The overall sound pressure level was calculated by performing an integration of the far-field SPL over a frequency range of $St_s = 0.2 - 18$. In general, Serration-2 configuration shows noise reduction compared to all the other configurations for both the presented angles of attack. At angle of attack $\alpha = 14°$, the No-Cusp also possesses similar OASPL values to Serration-2. Moreover, the reduction in OASPL for Serration-2 is only about 2-4 dB compared to the Baseline and Serration-1 configurations. At angle of attack $\alpha = 18°$, the Serration-2 exhibits substantial OASPL reduction of up to 10 dB compared

to the Baseline and Serration-1, whereas the No-Cusp shows a decrease in OASPL of up to 6 dB. The generation of the tonal peaks and noise reduction mechanisms of the serration configurations will be discussed in detail in the following sections.

D. Near-field spectral levels

The near-field unsteady pressure measurements were performed to gain further insight into the noise generation mechanism of the slat and slat cusp modifications. The unsteady surface pressure data were collected at various streamwise and spanwise locations on the surface of the slat (S1) and the main-element (FG1-FG5, M1-M4) of the high-lift airfoil using unsteady surface pressure transducers. The detailed locations of the transducers are presented in Table III. Simultaneous measurements of the near-field unsteady surface pressure fluctuations and far-field noise were carried out at angles of attack $\alpha = 14^\circ$ and 18°, for a free-stream velocity of $U_\infty = 30$ m/s, corresponding to a chord-based Reynolds number of $Re_c = 7.0 \times 10^5$.

Figure 11 shows the results for the unsteady surface pressure measurements from the transducer FG1 at the leading-edge of the main-element. In general, the near-field noise spectra for the Baseline case exhibits multiple distinct narrowband peaks for all the tested angles of attack with varying intensities, signifying the presence of cavity oscillation[36]. As expected, for the Baseline, the near-field spectra evidently shows the tonal peaks previously reported in Fig. 10, particularly two dominant peaks at $St_s = 1.6$ and 3.2 for both the angles of attack. A similar trend is also found in the case of Serration-1, with a slight reduction in the surface pressure level at the vortex shedding peak ($St_s = 1.5$) for the angle of attack $\alpha = 14^\circ$ and increased levels for the same peak at the angle of attack $\alpha = 18^\circ$. As seen in the far-field results, Serration-2 and No-Cusp configurations do not produce any narrowband peaks in the near-field spectra at angle of attack $\alpha = 14^\circ$, however, a peak with low energy is observed at $St_s = 2$ for $\alpha = 18^\circ$ for the No-Cusp configuration. Moreover, the wall pressure spectra at the angle of attack $\alpha = 14^\circ$, for the Serration-2 and No-Cusp, demonstrates increased SPL over the entire frequency range and specifically, in the low-mid frequency range ($St_s < 3$) at the angle of attack $\alpha = 18^\circ$. The increased spectral levels in the near-field surface pressure measurements for the Serration-2 and No-Cusp configurations relative to the Baseline are not observed in the far-field measurements in Fig.10, implying that the increased spectra in the near-field resulted from the non-propagating hydrodynamic energy field within the slat cove and

the main-element. Overall, it should be noted that the characteristic narrowband peak from the slat noise is completely eliminated for both the angles of attack in the case of Serration-2.

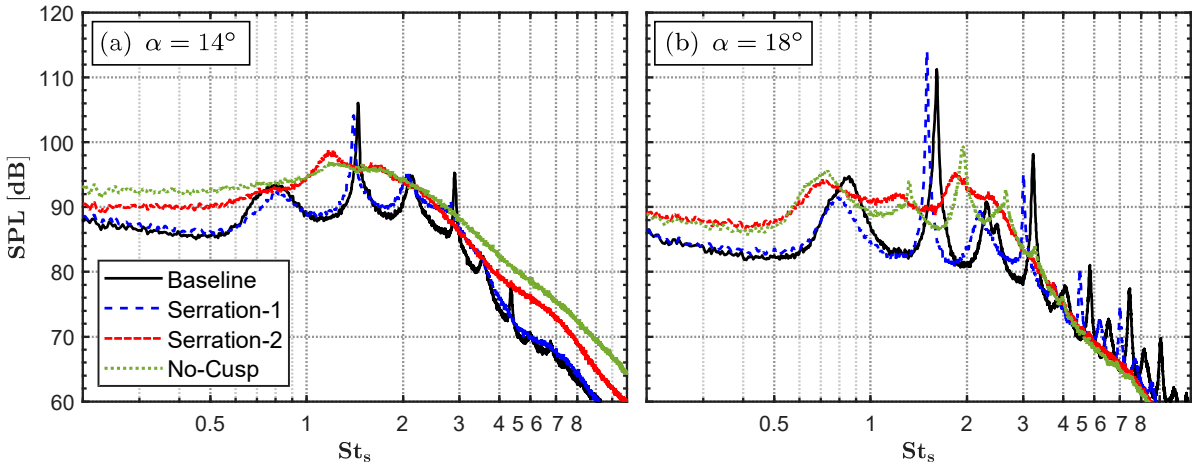

FIG. 11: Near-field point spectra for the FG1 transducer on the main-element as shown in Fig. 5 and detailed in Table III: (a) $\alpha = 14°$ and (b) $\alpha = 18°$.

The unsteady surface pressure measurements acquired from the remote sensors at the slat (S1) and the leading-edge of the main-element (M1-M4) are presented in Fig. 12. Considering the narrowband accuracy of the remote sensor, the results are presented only up to $St_s = 5.5$. Moreover, the far-field and unsteady surface pressure measurements from the Panasonic microphone and FG transducer in Figs. 10 and 11, respectively, show that the characteristic behavior of the slat tones lay within $St_s < 5.5$ and beyond $St_s > 5.5$, and the spectral results amongst all the tested cases follow a similar trend. The wall pressure fluctuation spectra exhibits multiple distinct narrowband peaks with varying intensities at the slat and the leading edge of the main-element for all the tested angles, similar to the results in Figs. 10 and 11. The wall pressure spectra trend between the two angles of attacks are similar, however, at angle of attack $\alpha = 18°$, the narrowband peaks are dominant and evident. Remote sensor S1, located at the slat region, exhibits the lowest energy level compared to the other sensors (M1-M4) at the leading-edge of the main-element for all the tested configurations. The application of Serration-1 on the slat results in a similar trend of the wall pressure fluctuations spectra compared to that of the Baseline, with marginally increased levels at the primary peak ($St_s \approx 1.6$) for the angle of attack $\alpha = 18°$, as seen earlier. No peaks are observed for the No-Cusp configuration at the angle of attack $\alpha = 14°$, however, at the angle of attack $\alpha = 18°$, peaks are generated at $St_s = 1.32$ for all the presented sensor locations, as mentioned above. The results

also show that Serration-2 can eliminate the vortex shedding peak at $St_s = 1.6$ for the angles of attack $\alpha = 14^\circ$ and 18° for all the presented sensor locations. Another important feature observed in Fig. 12 is the emergence of the spectral hump ($St_s = 0.6 - 1$) in the case of the Baseline and Serration-1 at angles of attack $\alpha = 14^\circ$ and 18°. Interestingly, the spectral hump is completely eliminated for the No-Cusp and Serration-2, particularly at the angle of attack $\alpha = 14^\circ$. However, at the angle of attack $\alpha = 18^\circ$, a mild spectral hump ($St_s = 0.6$) similar to the Baseline is observed for both the No-Cusp and Serration-2 configurations only at locations S1 and M1. The presence of spectral hump is observed to be more dominant in the near-field surface pressure measurements and weak in the far-field measurements in Fig. 10, implying that the increased spectra in the near-field emerges as a result of the non-propagating hydrodynamic energy field within the slat and main-element. Also, it is hypothesized that the broadband hump ($St_s = 0.5 - 0.9$) in this region, seen in the Baseline case, might be different in nature compared to the dominant even-numbered modes shown by kamliya *et al.*[36].

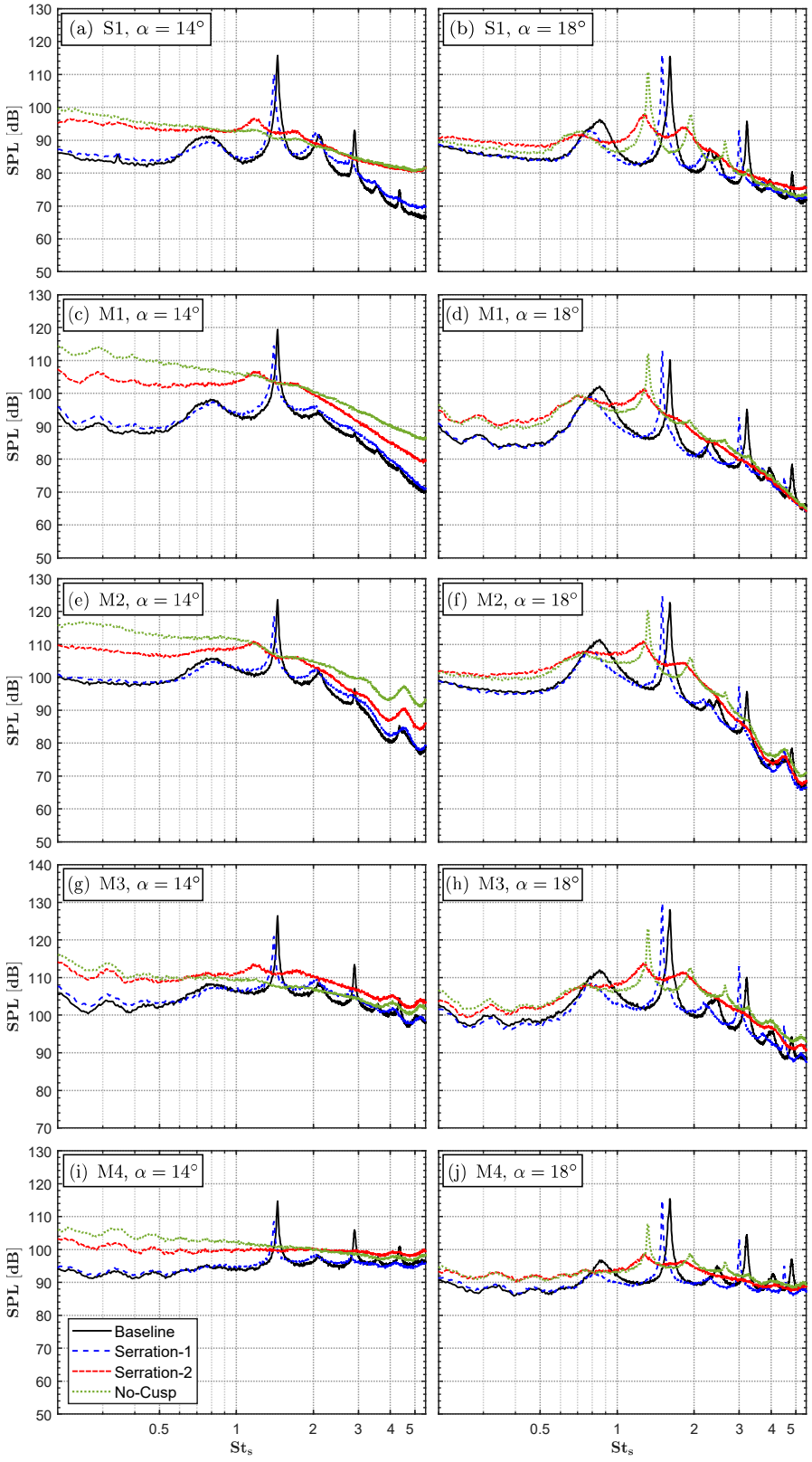

FIG. 12: Near-field point spectra for the remote sensor measurements shown in Fig. 5 and detailed in Table III: (a) S1, $\alpha = 14°$, (b) S1, $\alpha = 18°$, (c) M1, $\alpha = 14°$, (d) M1, $\alpha = 18°$, (e) M2, $\alpha = 14°$, (f) M2, $\alpha = 18°$, (g) M3, $\alpha = 14°$, (h) M3, $\alpha = 18°$, (i) M4, $\alpha = 14°$, and (j) M4, $\alpha = 18°$.

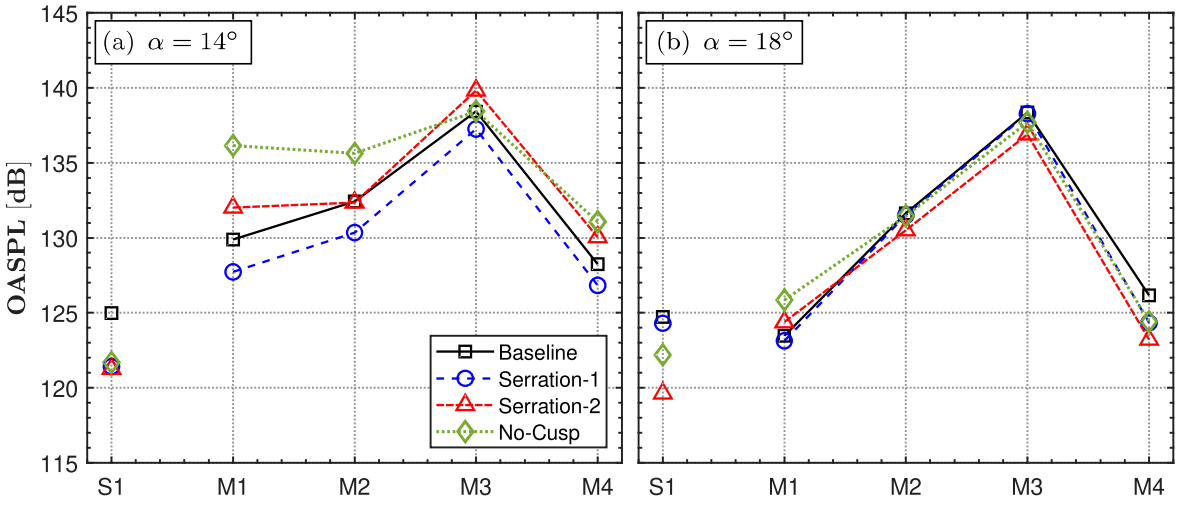

FIG. 13: Overall sound pressure level calculated from the near-field remote sensors on the slat and main-element: (a) $\alpha = 14°$ and (b) $\alpha = 18°$.

To provide a general quantitative estimation of the unsteady loading and to better understand the slat modifications, the overall sound pressure level (OASPL) of the near-field surface pressure fluctuations on the slat and main-element are calculated and presented in Figs. 13a and 13b for angles of attack $\alpha = 14°$ and $18°$, respectively. For the sensors, the overall sound pressure level was integrated for a frequency range of $St_s = 0.2 - 5.5$. For angle of attack $\alpha = 14°$, the results exhibit increased overall energy content for Serration-2 and No-Cusp compared to the Baseline and Serration-1, whereas, the Serration-1 case shows the lowest overall energy content compared to all the cases. For angle of attack $\alpha = 14°$, at S1, the Baseline experiences the highest overall energy level, whereas all the other configurations show a lower similar values. Furthermore, at the sensor locations M1, M2, and M4, the No-Cusp configuration demonstrates the highest overall energy content followed by Serration-2, Baseline, and Serration-1, respectively. Interestingly, only at location M3, Serration-2 exhibits marginally higher overall energy level followed by No-Cusp, Baseline, and Serration-1. Although the results for Serration-2 show higher overall energy content for the surface pressure fluctuations, the far-field overall energy content shows noise reduction for Serration-2 compared to the Baseline and Serration-1 configurations.

At angle of attack $\alpha = 18°$, Serration-2 is seen to cause a reduction in the overall energy level compared to all the other slat configurations. At the slat sensor location S1, the lowest overall energy level is found for Serration-2 followed by No-Cusp, although the Baseline and Serration-1

cases exhibit similar values. At S1, the Serration-2 configuration shows a reduction of up to 5 dB in overall energy level compared to the Baseline and Serration-1 configurations. Furthermore, at sensor location M2, M3, and M4, Serration-2 shows a reduction of up to 1-2 dB in the overall energy level compared to the other configurations with similar values. Interestingly, at location M1, the Baseline and Serration-1 reports lower overall energy content compared to the Serration-2 and No-Cusp configurations. Overall, the near-field overall energy content shows increased values for the Serration-2 configuration at angle of attack $\alpha = 14°$, whereas at angle of attack $\alpha = 18°$, Serration-2 exhibits reduced overall energy level compared to all the other configurations. It should be noted that the far-field OASPL indicated noise reduction for Serration-2, therefore, the increase in overall energy level in the near-field could be attributed to the non-propagating hydrodynamics of the flow-field.

1. Auto-correlation

The dominant time scales in the flow can be determined by performing an auto-correlation analysis on the unsteady surface pressure fluctuations within the slat cove region. The auto-correlation were calculated using the unsteady surface pressure from,

$$R_{p_i p_i}(\tau) = \frac{\overline{p_i(t+\tau)p_i(t)}}{p^2_{i_{RMS}}}, \tag{1}$$

where p_i is the surface pressure, $p_{i_{RMS}}$ is the surface pressure root-mean-squared, τ is the time delay and the time average is represented by the overbar.

The auto-correlation of the surface pressure at the remote sensor location S1 (slat) and M1 (main-element) for the Baseline, Serration-1, Serration-2, and No-Cusp configurations at the angle of attack $\alpha = 14°$ and $18°$ are presented in Fig. 14. The auto-correlation $R_{p_i p_j}(\tau)$ results are presented as a function of the normalized time delay $\tau U_\infty / c_s$. In the case of the sensor on the slat (S1), the $R_{p_i p_j}(\tau)$ results for the Baseline and Serration-1 cases exhibits a slow decaying periodic behavior with a Gaussian shape at both the angles of attack (14° and 18°), indicating the emergence of a strong vortex shedding[36]. The $R_{p_i p_i}(\tau)$ results of the Serration-2 and No-Cusp cases shows a very weak periodic shape that exhibits a fast decaying periodic behavior, signifying the absence of a strong vortex shedding for the angle of attack $\alpha = 14°$, in accordance with the results in Figs. 11 and 12. Conversely, in the case of the No-Cusp configuration, at angle of attack $\alpha = 18°$, the $R_{p_i p_i}(\tau)$ shows a stronger periodic behavior, signifying the presence of vortex shedding. The

$R_{p_ip_i}(\tau)$ for the Serration-2 configuration exhibits a weaker periodic behavior compared to all the tested cases at the angle of attack 18°.

It is well established that the distance between the two peaks in the $R_{p_ip_i}(\tau)$ for the Baseline case shown in Fig. 14(b) corresponds to the vortex shedding frequency ($\tau^*_{vs} = \tau U_\infty/c_s$). Furthermore, the time delay found in the Baseline case is $\tau^*_{vs} \approx 0.625$, corresponding to $St_s = 1.6$, associated with the fundamental vortex shedding peak observed in Figs. 11 and 12. At the leading edge of the main-element (M1), the $R_{p_ip_j}(\tau)$ results for the Baseline and Serration-1 cases exhibit a slow decaying periodic behavior with a low decay rate at both the angles of attack, similar to the slat location S1. For the Serration-2 and No-Cusp configurations, at the angle of attack $\alpha = 14°$, the $R_{p_ip_j}(\tau)$ results shows a very weak periodic shape that decays instantaneously, indicating the absence of a strong vortex shedding. At the angle of attack $\alpha = 18°$, the $R_{p_ip_j}(\tau)$ for all the tested cases (i.e. Baseline, Serration-1, Serration-2 and No-Cusp) reveal a fast decaying periodic behavior. The amplitude of the $R_{p_ip_j}(\tau)$ results for the angle of attack $\alpha = 18°$ is much smaller compared to $\alpha = 14°$, signifying the emanation of lower energy of the vortex shedding in the vicinity of the main-element leading edge. Overall, the suppressed $R_{p_ip_i}(\tau)$ periodic behavior for the Serration-2 configuration indicates the suppression of the vortex shedding. Moreover, the strong $R_{p_ip_i}(\tau)$ periodic behavior observed for No-Cusp configuration also further signifies the role of the Serration-2 at the slat cusp to eliminate the vortex shedding and thus, the feedback mechanism.

E. Coherence studies

1. Streamwise coherence

In order to better understand the dynamics of the flow structures within the slat and near the leading-edge of the main-element, near-field coherence studies were carried out. The coherence of the signals was determined by the phase correlation between two different remote sensors in the streamwise locations, averaged over time, and can be found from;

$$\gamma^2_{p_ip_j}(f) = \frac{|\ \Phi_{p_ip_j}(f)\ |^2}{\Phi_{p_ip_i}(f)\Phi_{p_jp_j}(f)} \quad \text{for } p_i = \text{ M1 and } p_j = \text{ M2, M3, M4,} \tag{2}$$

where M1 is the reference sensor, while M2-M4 are the downstream sensors mounted on the leading-edge of the main-element. The locations of the remote sensors are provided in Table III.

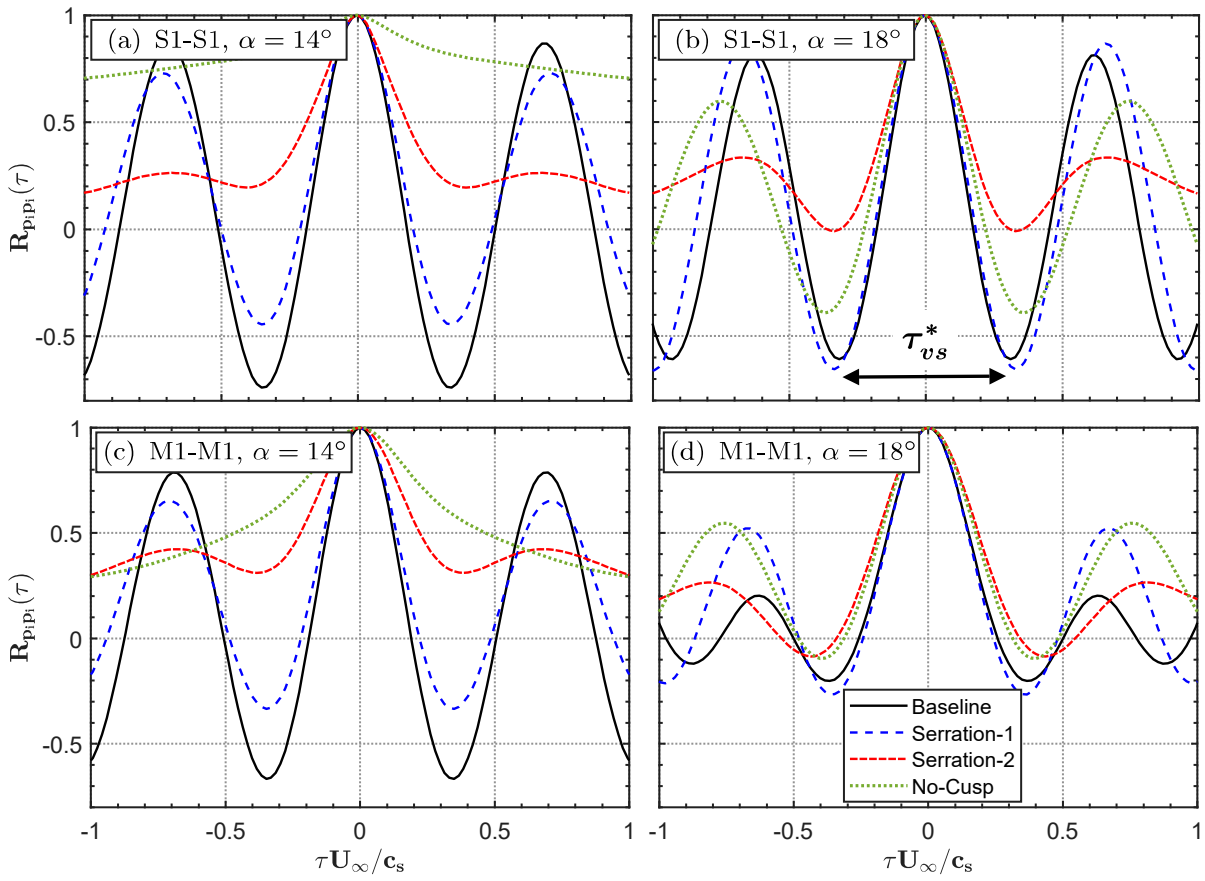

FIG. 14: Auto-correlation of the remote sensors at the slat location S1 and main-element location M1: (a) S1-S1, $\alpha = 14°$, (b) S1-S1, $\alpha = 18°$, (c) M1-M1, $\alpha = 14°$, and (d) M1-M1, $\alpha = 18°$.

Figure 15 shows the coherence ($\gamma^2_{p_ip_j}$) between the reference sensor M1 and the other sensors M2-M4 on the streamwise direction for the four tested configurations (i.e. Baseline, Serration-1, Serration-2, and No-Cusp) at the angles of attack $\alpha = 14°$ and $18°$. In general, the results show high coherence between the sensors M1-M2 for all the tested configurations at both the angles of attack over most of the frequency range, except over frequencies $St_s > 3$. The broadband coherence spectra at $St_s > 3$ for the Serration-1, Serration-2 and No-Cusp configurations are much higher than that of the Baseline case at $\alpha = 14°$. For M1-M3, the highest coherence levels are observed for the Baseline and Serration-1 over the entire frequency range at the angle of attack $\alpha = 14°$, however, at the angle of attack $\alpha = 18°$, a fairly similar coherence is observed amongst all the cases. In particular, high coherence levels are found at the tonal peaks, specifically at the primary peak ($St_s = 1.6$). Additionally, the coherence between M1-M3 also reveals the suppression of the fundamental peaks along with its harmonic by the Serration-2 configuration especially at $\alpha = 14°$. For M1-M4, in the

case of Serration-2 and No-Cusp, coherence levels were found to be almost zero. However, at the angle of attack $\alpha = 18°$, the coherence levels (M1-M4) reveal similar coherence over the broadband range of the spectra amongst the three configurations excluding the tonal peaks, indicating that they all have similar three-dimensional flow structures. A notable reduction in coherence levels is found for the Serration-2 configuration compared to other cases, in accordance with the results observed in the surface pressure spectra (see Fig. 11(b)). Moreover, for all the streamwise coherence locations in Fig. 15, high coherence levels are found at $St_s = 0.6$, indicating the emergence of spectral humps for all the presented configurations and angles of attack. Interestingly, a significant reduction in the coherence levels for the broadband spectral hump at low frequencies and the tonal peaks can be observed for the Serration-2 and No-Cusp configurations, especially at the angle of attack $\alpha = 14°$. Overall, the streamwise coherence results show a reduction in flow energy at consecutive streamwise locations for Serration-2 and No-Cusp with reduced coherence levels compared to the highly energetic Baseline and Serration-1.

2. Spanwise correlation length scale

The spanwise correlation length of wall pressure fluctuations was studied to determine the noise generated through the interaction of pressure signals in the spanwise direction in the slat vicinity. The spanwise correlation length scale (Λ_γ) of the spanwise flow structures was calculated using the spanwise coherence (γ) results between the surface pressure transducers (FG1-FG5) at various lateral spacing (Δz) and can be found from,

$$\Lambda_\gamma(f) = \int_0^\infty \gamma_{p_i p_j}(f, \Delta z)\, d\Delta z. \tag{3}$$

Figure 16 shows the correlation length scale (Λ_γ) as a function of frequency (St_s) for the Baseline, Serration-1, Serration-2 and No-Cusp configurations at the angles of attack $\alpha = 14°$ and $18°$. For the angle of attack $\alpha = 14°$, the Baseline and Serration-1 follow a similar trend over the same length scales with an exception of tonal peaks at high frequencies ($St_s > 3$) for Serration-1, where the tones were suppressed. The highest length scale was found at the primary tonal peak at about Λ_γ/c_s =0.082. Furthermore, the results report that the spanwise length scales could be significantly reduced by Serration-2 and No-Cusp configurations at the spectral hump and multiple peaks, with an average correlation length scale of about $\Lambda_\gamma/c_s \approx 0.02$. Additionally, the application of Serration-2 notably reduced the length scale at the primary tonal peak ($St_s = 1.6$) with a slight

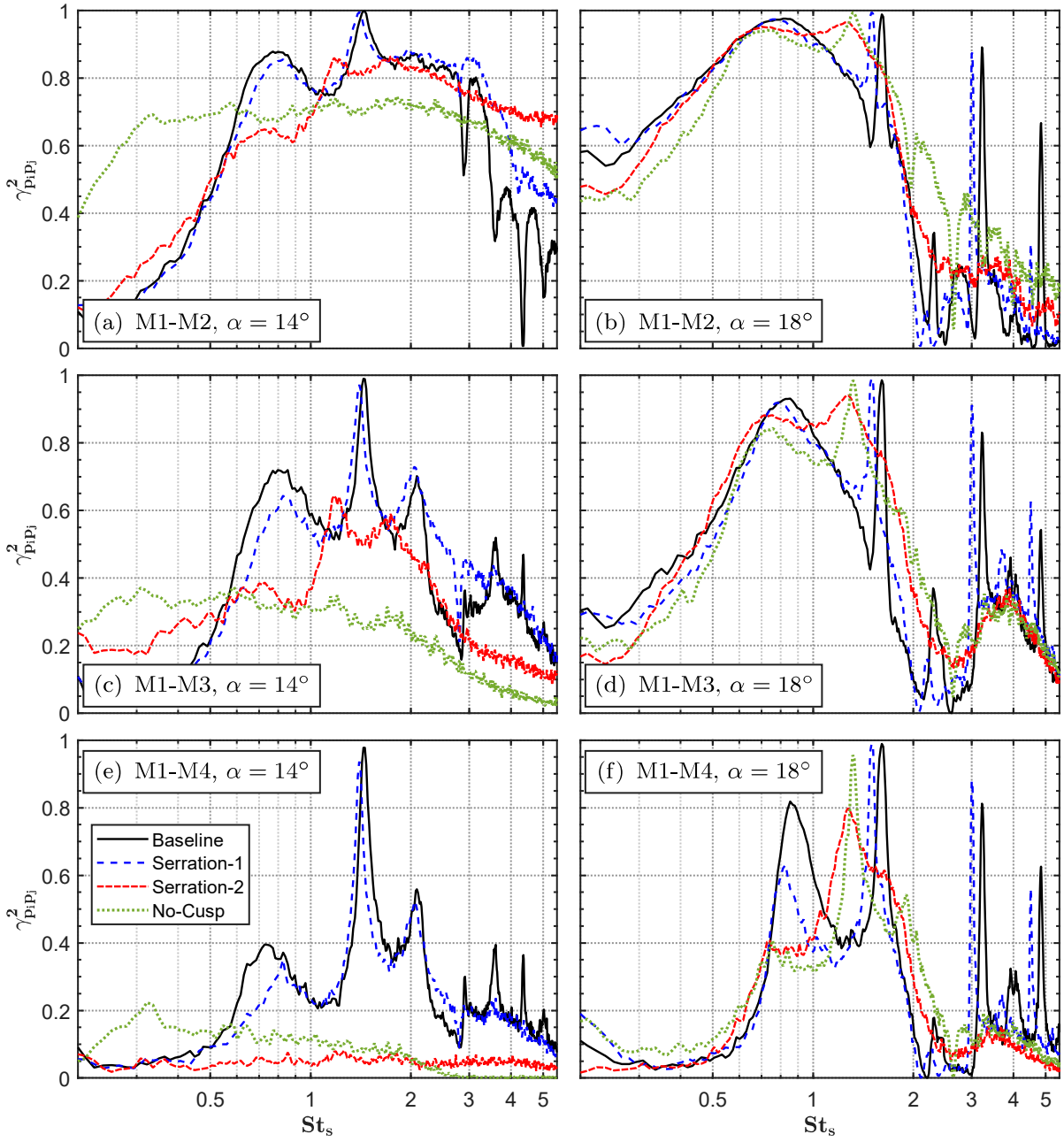

FIG. 15: Streamwise coherence between the sensors located at the leading-edge of the main-element: (a) M1-M2, $\alpha = 14°$, (b) M1-M2, $\alpha = 18°$, (c) M1-M3, $\alpha = 14°$, (d) M1-M3, $\alpha = 18°$, (e) M1-M4, $\alpha = 14°$, and (f) M1-M4, $\alpha = 18°$.

shift to the lower frequency range. For all the tested configurations, at angle of attack $\alpha = 18°$, the correlation length scales over the whole frequency range are much larger than that of those found at the angle of attack $\alpha = 14°$. Moreover, at $\alpha = 18°$, the length scales demonstrate two distinct peaks at the spectral hump for the Baseline and No-Cusp configurations. Furthermore,

at the mid to high-frequencies ($St_s > 2$), the Baseline, Serration-1, and No-Cusp configurations also demonstrate a similar broadband trend. However, in the case of Serration-2, the spanwise correlation length remains almost the same between $St_s = 2$ and $St_s = 4$ but reduced at higher frequencies $St_s > 4$. Overall, the spanwise correlation length for the Serration-2 case reaffirms the elimination of the tonal behavior generated due to the acoustic feedback mechanism within the cavity.

3. Near- to the far-field coherence

In order to distinguish the non-propagating hydrodynamic field and the noise radiated to the far-field, the coherence between the near-field surface pressure sensors on the high-lift device and the far-field microphone above the slat trailing-edge were carried out. The near- to the far-field coherence was calculated using the following equation,

$$\gamma^2_{p_i p_j}(f) = \frac{|\ \Phi_{p_i p_j}(f)\ |^2}{\Phi_{p_i p_i}(f)\Phi_{p_j p_j}(f)} \quad \text{for } p_i = \text{ S1, M1 and } p_j = \text{FF}^{90^\circ}, \tag{4}$$

where $|\cdot|$ is the absolute value, S1 and M1 are the reference sensors on the slat and the leading-edge of the main-element, respectively, and FF^{90° is the far-field microphone at a distance of 1 m and 90° away from the slat trailing edge. The $\Phi_{p_j p_j}$ is the cross-spectral density between the two pressure signals p_i and p_j.

The coherence $\gamma^2_{p_i p_{90^\circ}}$ between the near-field remote sensors on the slat and the main-element of the high-lift airfoil (S1, M1) and the far-field microphone (FF^{90°) for the Baseline, Serration-1, Serration-2 and No-Cusp configurations at the angles of attack $\alpha = 14^\circ$ and 18° are presented in Fig. 17. In general, high coherence levels are observed at all tonal peaks that appear as a result of the cavity oscillations, in line with a previous study by Kamliya *et al.*[36]. For the angle of attack $\alpha = 14^\circ$, marginally increased coherence levels are observed in the case of S1-FF^{90° over the entire frequency range compared to the M1-FF^{90° for all the tested configurations. Evidently, the coherence levels observed in the Baseline and Serration-1 at the broadband hump ($St_s = 0.5 - 0.9$), the vortex shedding peak ($St_s \approx 1.6$), and the other distinct narrowband peaks are eliminated for the No-Cusp configuration with coherence values below $\gamma^2_{p_i p_{90^\circ}} < 0.1$. Furthermore, both the broadband hump, with high coherence levels at about $0.5 < St_s < 0.9$ and the vortex shedding peak at $St_s \approx 1.6$ are significantly reduced with the application of Serration-2. At the angle of attack $\alpha = 18^\circ$, for

both the near-field pressure sensor on the slat (S1) and the main-element (M1), high coherence levels were found over the entire frequency range. Contrary to the coherence levels observed at the angle of attack $\alpha = 14°$, the No-Cusp configuration exhibits high coherence levels, particularly at the fundamental tonal peak ($St_s = 1.6$) with a slight shift to a lower frequency value. Overall, the results in Figs. 17(b) and (d) show that the near-to-far-field coherence ($\gamma^2_{p_i p_{90°}}$) at the broadband hump, the vortex shedding peak, and the other distinct narrowband peaks could be significantly reduced by the application of the Serration-2 when compared to that of the Baseline, Serration-1, and No-Cusp configurations. Finally, this section confirms that the increased noise observed for the Serration-2 and No-Cusp configurations in the near-field measurements, seen earlier in Fig.12, is solely due to the near-field non-propagating hydrodynamic field since the overall coherence of these configurations remain low over a wide range of frequencies.

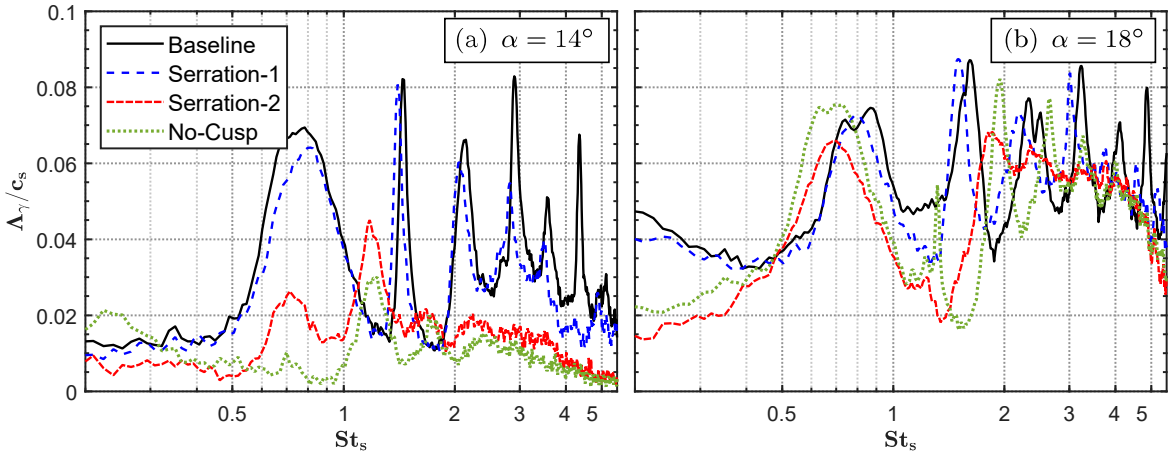

FIG. 16: Spanwise coherence length scales based on the unsteady surface pressure transducers measurements (FG1-FG5): (a) $\alpha = 14°$, and (b) $\alpha = 18°$.

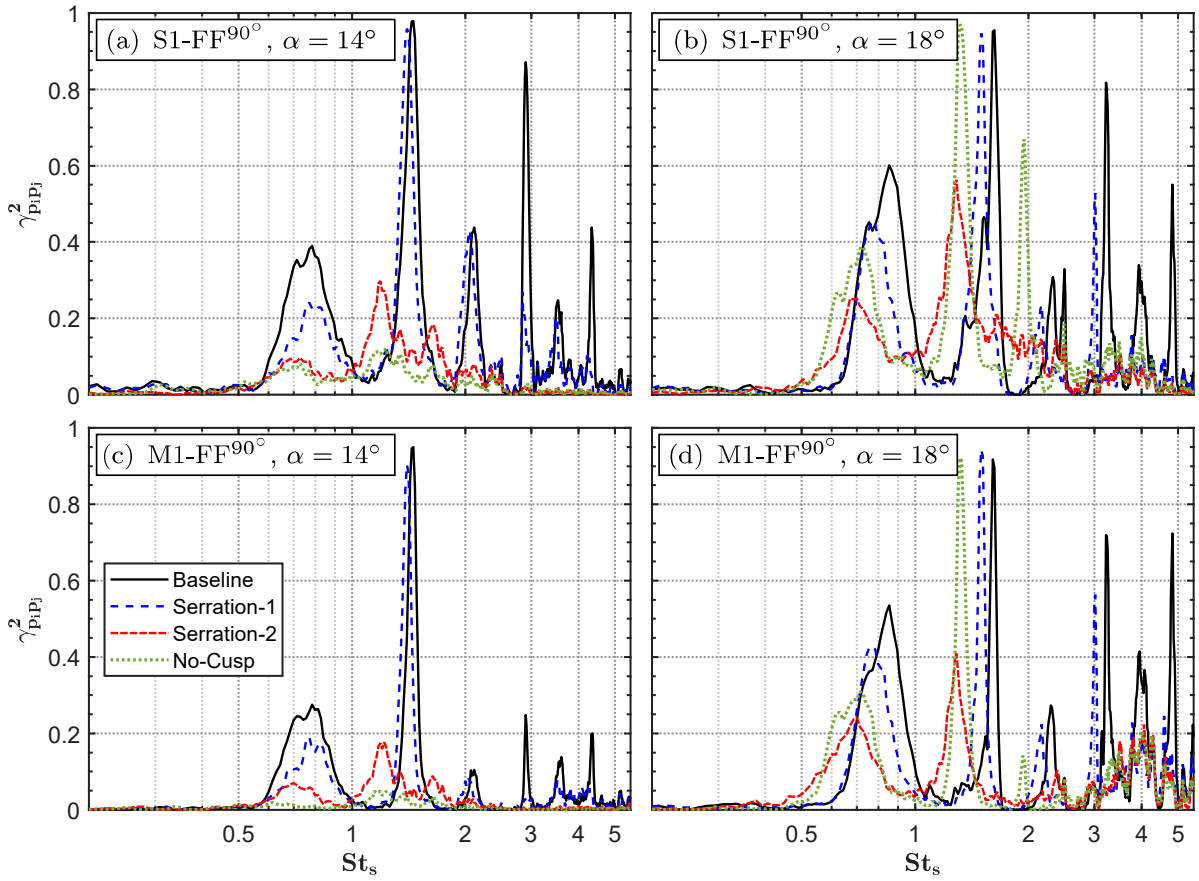

FIG. 17: Coherence between the near-field sensors at the slat location S1 and main-element location M1 with the far-field microphone at 90° placed 1 m away from the slat trailing edge: (a) S1-FF$^{90^\circ}$, $\alpha = 14°$, (b) S1-FF$^{90^\circ}$, $\alpha = 18°$, (c) M1-FF$^{90^\circ}$, $\alpha = 14°$, and (d) M1-FF$^{90^\circ}$, $\alpha = 18°$.

F. Statistical Analysis

In order to characterize the turbulent motions of flow within the slat cavity with and without the serrated slat cusp, statistical moments of the turbulence distribution are studied using the probability density function (PDF), skewness and kurtosis. Figure 18 shows the probability density function (PDF) of the surface pressure fluctuations at the slat (S1) and the leading edge of the main-element (M1-M4) at the angle of attack $\alpha = 18°$. The surface pressure fluctuation values were normalized by the standard deviation at each pressure level. In principle, PDF with a Gaussian distribution is assumed for velocity fluctuations dominated by homogeneous turbulence. Similarly, the univariate statistical analysis of unsteady pressure fluctuations could also be used to determine

the relative flow conditions. Therefore, a normalized Gaussian distribution is included in the figure for comparison. It was found that, at the slat region (S1), the PDFs of the surface pressure fluctuations gradually skew toward the negative side, with an increase of wall-normal distance for Baseline, Serration-1, and No-Cusp configurations whereas the PDF of the Serration-1 move closer to Gaussian distribution. As for the sensor at the leading edge of the main-element M1, the PDF curves show a quasi-Gaussian distribution for all the cases, whereas Serration-2 exhibits a Gaussian distribution. For the sensor M2, the PDFs are dominated by positive pressure events, whereas for M3, they are dominated by negative pressure events for all the configurations. Furthermore, the PDF results, for the remote sensor M4, for all the tested cases, also reveals the distribution dominated by negative pressure events. Interestingly, significant deviation with a well-distributed positive tail is also observed, with Serration-2 having the highest deviation followed by No-Cusp, Serration-1, and Baseline. Moreover, the larger number of points past the six standard deviations from the mean indicates a much higher probability for values in this region than a normal distribution could predict. Furthermore, when the distribution of pressure fluctuations deviates from Gaussian, it denotes that the pressure events are dominated by flow characteristic features such as vortex shedding and when the distribution is Gaussian, the flow is turbulent. Considering this, the PDF observations could be better interpreted using third and fourth-order moments such as skewness and kurtosis. For a stochastic signal x, skewness (s) and kurtosis (k) can be defined as,

$$s = \frac{EV(x-\mu)^3}{\sigma^3}, \tag{5}$$

$$k = \frac{EV(x-\mu)^4}{\sigma^4}, \tag{6}$$

where μ and σ are the mean and standard deviation of the pressure signal, respectively and EV[$\cdot$] is the expected value.

Figure 19 shows the results of skewness and kurtosis for all the configurations at the angle of attack 18°. Skewness measures the asymmetry of the data signal distribution around the sample mean. Predominantly, the data exhibits a Gaussian distribution when the skewness value is close to zero. For the presented results, the positive and negative skewness values indicate the events dominated by positive and negative pressure, respectively. In general, the skewness exhibits significant differences at various sensor locations for all the configurations. The skewness values, for Serration-2, are evidently close to zero at all the sensor locations compared to the other configurations, except

at M2. A similar trend is observed for the No-Cusp configurations. Kurtosis, on the other hand, measures whether the data are peaked or flat relative to the normal distribution. In the case of kurtosis, the data exhibits a Gaussian distribution when the kurtosis of the normal distribution is 3. The results reveal that all the cases had a kurtosis value below 3 for the pressure transducers M1, M2, and M3, signifying the occurrence of platykurtic distribution with fewer values in the tails and close to the mean. The platykurtic distribution trend can also be seen in Figs. 18(c) and (d), where the PDFs of all the tested configurations exhibit fewer values in the tails and are much closer to the mean compared to the other slat and main-element region. The results obtained here could also be possibly related to the presence of persistence turbulence associated with the peak on the near field spectral analysis observed in Fig. 12. Additionally, remote sensor M4 exhibits high kurtosis values including a distinct peak near the mean with heavy tails. Overall, also in the case of kurtosis, Serration-2 shows values closer to or at 3 for all the remote sensor locations, compared to all the cases except at location M4. Ultimately, this analysis shows that persistent flow characteristics such a vortex shedding, well known to exist in normal slat configuration, are eliminated by the use of Serration-2. Moreover, the stochastic characteristics of the pressure events appear to be comparatively different for the Serration-2 at location M4 past the slat trailing edge post slat impingement, reaffirming the substantial change in the flow characteristics caused by Serration-2 configuration.

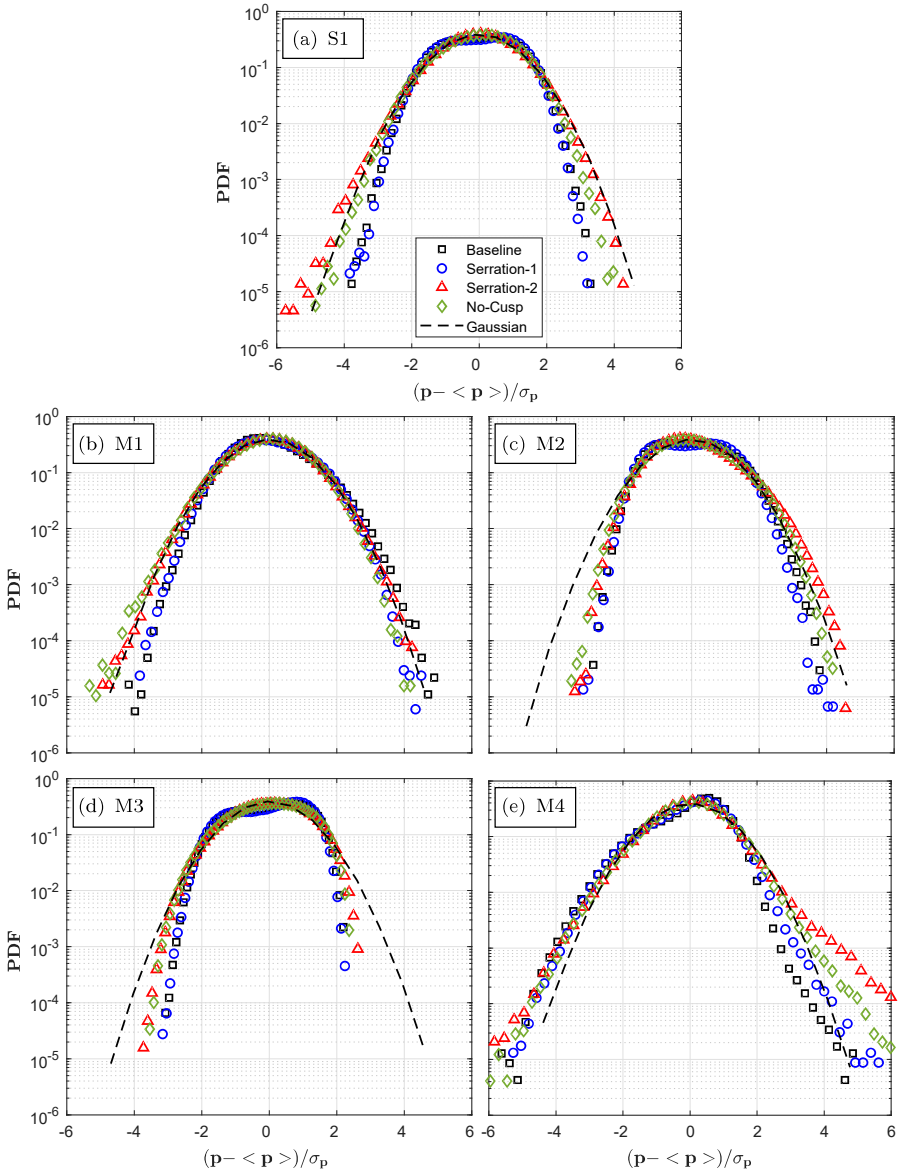

FIG. 18: Probability density functions of the surface pressure fluctuation at the slat location (a) S1, and the leading edge of the main-element (b) M1, (c) M2, (d) M3, and (e) M4 for angle of attack $\alpha = 18°$.

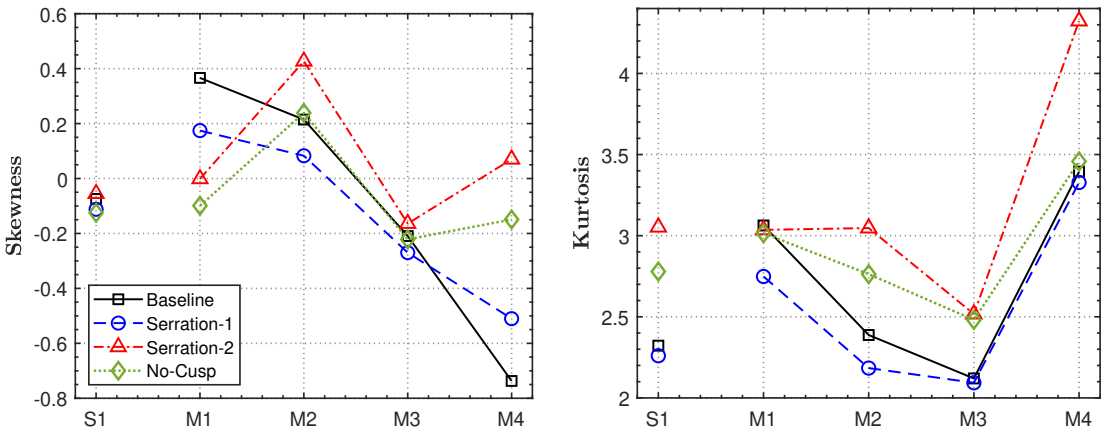

(a) Skewness

(b) Kurtosis

FIG. 19: (a) Skewness and (b) Kurtosis at angle of attack $\alpha = 18°$ for the remote sensor measurements on the slat (S1) and main-element (M1-M4) show in Fig. 5.

G. Higher order spectral analysis

1. Auto-bicoherence spectrum

In order to resolve the quadratic and phase coupling of the pressure signals with itself, the non-linear energy transfer between the frequencies can be calculated using the auto-bispectrum (B_{ppp}). The auto-bispectrum can be found from, $B_{ppp}(f_i, f_j) = \lim_{T\to\infty} \frac{1}{T} EV[P(f_i)P(f_j)P^*(f_i + f_j)]$, where $P(f)$ is the Fourier Transform of $p(t)$, T is the time length, $EV[\cdot]$ is the expected value and $*$ denotes the complex conjugate. The results here will be presented by normalizing the auto-bispectrum by its corresponding power spectrum elements, known as the auto-bicoherence, calculated as follows,

$$b^2_{ppp}(f_i, f_j) = \frac{|\, B_{ppp}(f_i, f_j)\,|^2}{\Phi_{pp}(f_i + f_j)\Phi_{pp}(f_i)\Phi_{pp}(f_j)}. \tag{7}$$

The frequency components of the wave (f_i, f_j and $f_i + f_j$) are statistically independent if the auto-bicoherence $b^2_{ppp} = 0$. The auto-bicoherence is below 1 (i.e. $0 < b^2_{ppp} < 1$) if the frequency component at $f_i + f_j$ demonstrate any phase relationship with f_i and f_j, while a perfect quadratic coupled waves is found when $b^2_{ppp} = 1$.

Figure 20 shows the auto-bicoherence contours for the surface pressure transducer FG1 on the

leading edge of the main-element at the angle of attack $\alpha = 18^\circ$ for the Baseline, Serration-1, Serration-2, and No-Cusp configurations. It should be noted that the figures are marked with the mode numbers (St_{1-8}) corresponding to the peaks observed in the near-field measurements in Fig. 11. The results for the Baseline show that the multiple peaks observed in Fig. 11(b) have quadratic coupled modes caused by self-interaction of the modes in the slat cavity, i.e., the primary peak $St_s = 1.6$ ($St_{(2-2)}$), and at the corresponding harmonics ($St_{(4-4)}, St_{(6-6)}, St_{(8-8)}$). For modes with St_6 and St_8, the bicoherence value is about $b^2_{ppp} > 0.8$, implying the formation of these harmonics $St_6 = 3St_2$ and $St_8 = 4St_2$ through quadratic coupling[36]. Moreover, for the even modes at $St_{2,4,6}$, the results show the possibility of phase coupling with all the other modes excluding odd modes, St_3, St_5, and St_7. Interestingly, self-interaction is absent in the case of the spectral hump at St_1 ($St_s = 0.6$) observed in Fig. 11(b), implying that the broadband hump is independent and is not quadratically coupled. The bicoherence contours, for the Serration-1 configuration, exhibit similar behavior to that of the Baseline case but with a few weak quadratic coupled modes, particularly at the primary modes (St_2) with the other odd and even modes (i.e. St_4 and St_6), respectively. In the case of the No-Cusp configuration (Fig. 20(d)), strong self-interaction quadratic coupled modes are observed at $St_{(2-2)}$) and ($St_{(3-3)}$). Moreover, the No-Cusp configuration indicates a slight shift to the higher St_s compared to those of the Baseline case, consistent with the peaks observed in Fig. 11(b). Finally, Serration-2 shows no tonal interaction even for small peaks observed in Fig. 11(b). Moreover, they exhibit self-interaction with low bicoherence levels for the broadband hump observed in the near-field surface pressure results in Fig. 11(b). Subsequently, a weaker self-interaction emerges at St_2, further reaffirming that the application of Serration-2 can significantly eliminate the fundamental peak and weaken the constructive self-interaction of the modes compared to that of the Baseline configuration.

2. Persistence spectrum

The nature of the multiple distinct narrowband peaks observed in Fig. 11 was further analyzed using the persistence spectrum to visualize the energy distribution of the signals over time along with phase coupling of the signal. In principle, the persistence spectrum reveals the energy density in time as a percentage for a given signal in the frequency spectrum. For this purpose, the persistence spectrum was calculated and presented for the surface pressure signals obtained by the transducer

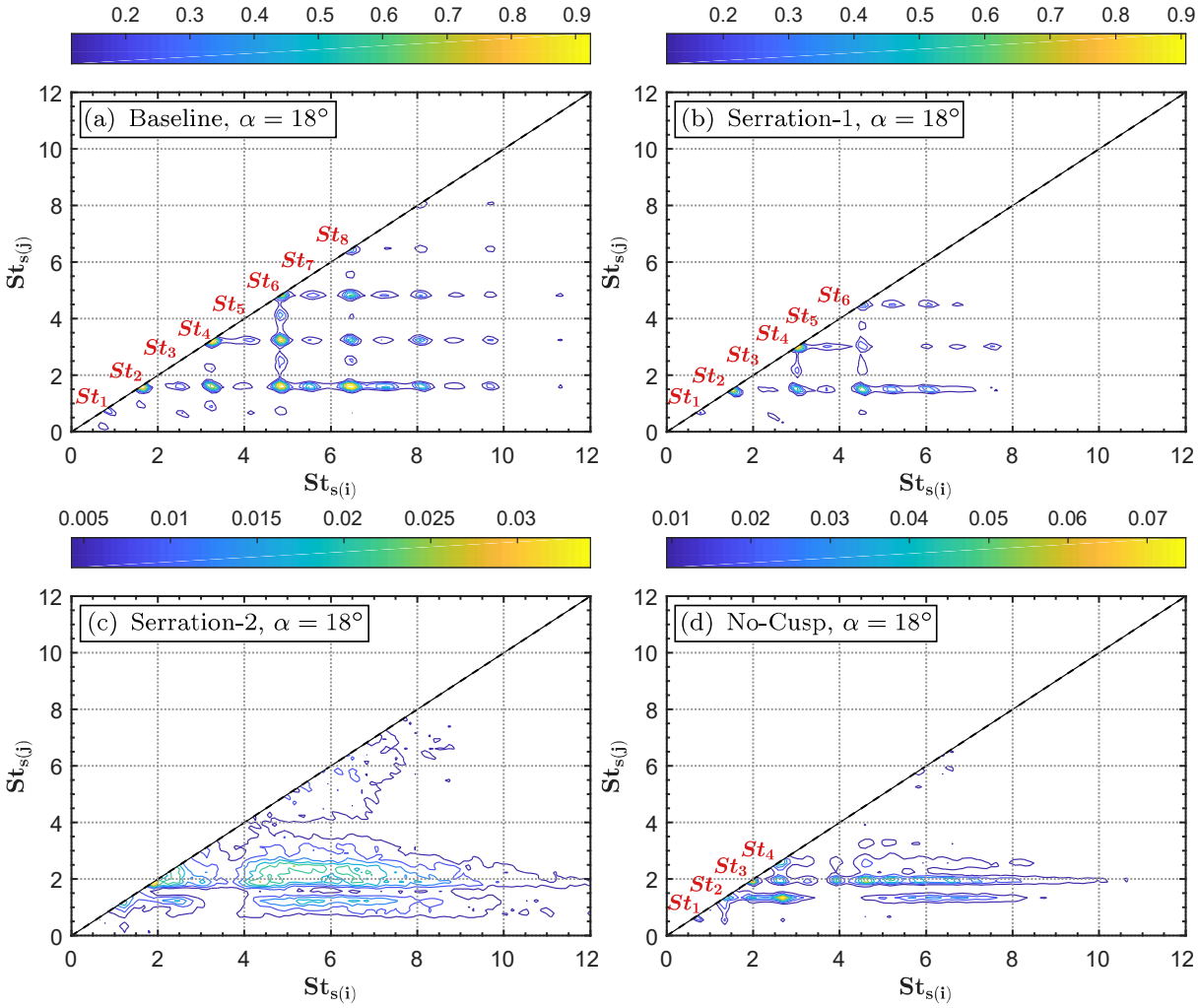

FIG. 20: The auto-bicoherence contours for the surface pressure transducer FG1 on the main-element at angle of attack $\alpha = 18°$ for (a) Baseline, (b) Serration-1, (c) Serration-2, and (d) No-Cusp configurations.

FG1. The measurements were performed for 120 s, with a time and frequency resolution of 0.04 s and $St_s = 0.45$, respectively. The contour plots of the spectrum were obtained using the multiple Short-Time Fourier Transform (STFF) presented over each other. Figure 21 shows the persistence spectrum for all the tested configurations (i.e. Baseline, Serration-1, Serration-2 and No-Cusp) at the angle of attack of $\alpha = 18°$. For the Baseline and Serration-1, the results demonstrate the presence of primary acoustic energy with the highest energy content persistent over time at the vortex shedding frequency ($St_s \approx 1.6$) and the harmonics of the fundamental peak. Moreover, the peaks with the highest energy content are densely distributed in time as seen from the contours,

where the tonal frequency (i.e. $St_s \approx 1.6$) persists in a signal for the longest period. In line with the auto-bicoherence results in Fig. 20, significantly lesser energy levels are observed in the peak distributed over time at the odd St_s modes, implying that these modes do not have any phase relation with the even modes. The results for the No-Cusp case, on the other hand, exhibit maximum energy content at $St_s = 1.9$, as seen in Fig. 11(b). In the case of Serration-2 configuration, the spectrum shows that the pressure signal is of a broadband nature over the entire period. It can be observed that the emergence of the broadband spectral hump in Fig. 11(b) at $St_s = 0.6-1$ for all the cases is not persistent but well distributed in time. Ultimately, the results from the persistence spectrum further clarify that the characteristic slat flow features such as the vortex shedding and the broadband hump at $St_s = 0.6-1$ are eliminated by the application of Serration-2, furthermore, the results point out the flow to be broadband and well distributed in time.

3. Wavelet spectrum

In order to better understand the temporal characteristics of the pressure signals and their associated frequency, the continuous wavelet transform (CWT) method has been employed in the present study. In recent studies[28,29,36], continuous wavelet transforms have been used to analyze the amplitude modulation mechanics associated with the multiple narrowband peaks generated by the high-lift airfoils. Furthermore, Farge[54] has shown that the turbulence characteristics of a flow field can be classified using wavelet analysis. The continuous wavelet transform (CWT) is calculated from,

$$W_x(a,\tau) = \frac{1}{\sqrt{C_\psi}} \int_{-\infty}^{+\infty} x(t)\, \psi^*_{a,\tau}\Big(\frac{t-\tau}{a}\Big)\, \mathrm{d}t, \tag{8}$$

where $W_x(a,\tau)$ is the continuous wavelet transform of function $x(t)$, $a > 0$ is the scale variable, τ is the time delay, a is the scale dilation parameter, $\psi_{a,\tau}(t)$ is the wavelet function, $1/\sqrt{C_\psi}$ is a constant that takes the mean value of $\psi(t)$ into account and $\psi^*\big(\frac{t-\tau}{a}\big)$ is the complex conjugate of the dilated and translated mother wavelet $\psi(t)$. Based on previous studies[36,55,56] Morlet kernel was chosen as the mother wavelet. The measurements of the CWT in the present study were performed for 120 s and the results are presented for 0.6 s for better visualization.

Figure 22 shows the contour plots of the wavelet coefficient modulus of the unsteady surface pressure signals at the sensor M3 on the leading edge of the main-element for the Baseline, Serration-

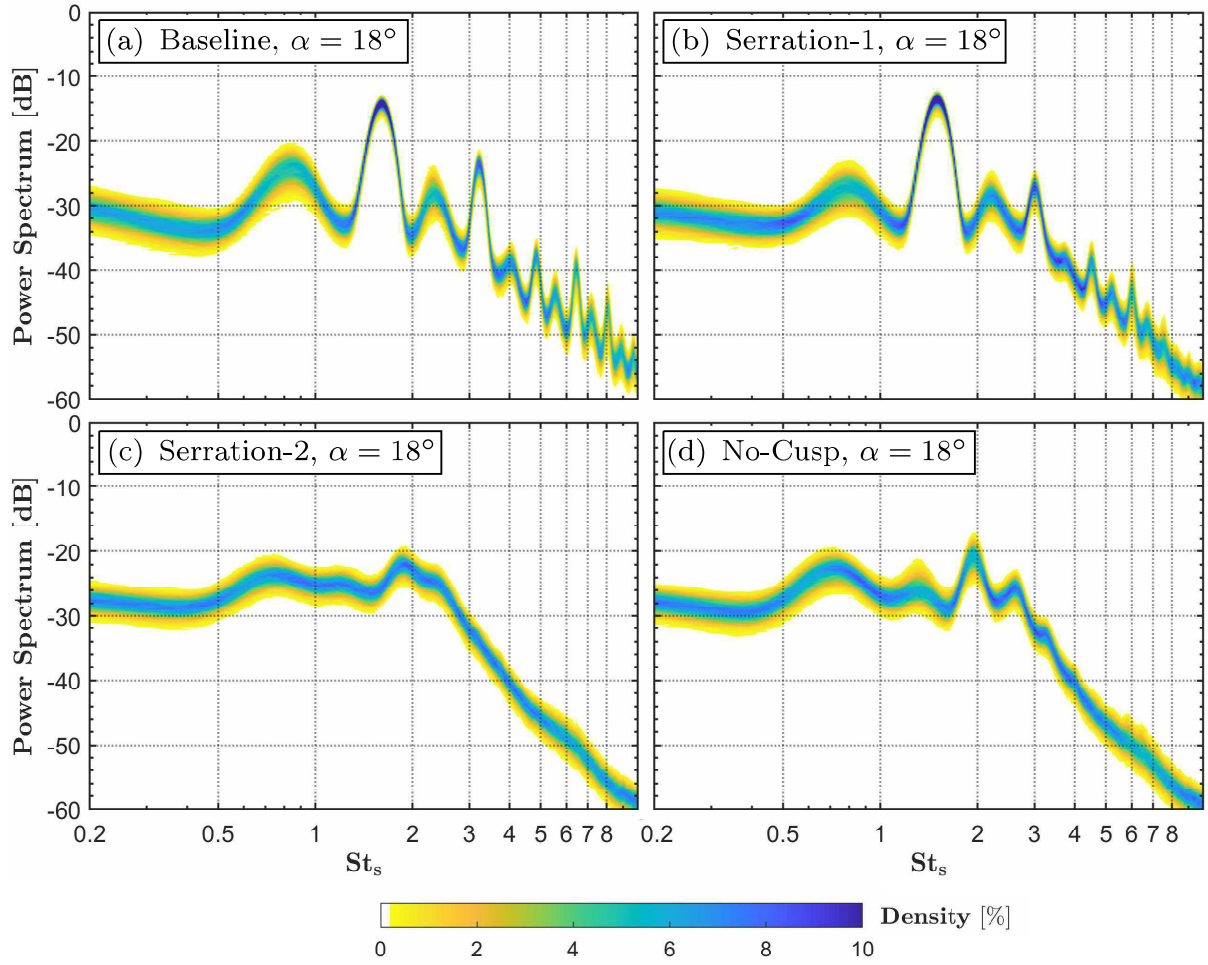

FIG. 21: The persistence spectrum contour for the surface pressure transducer FG1 on the main-element at angle of attack $\alpha = 18°$ for (a) Baseline, (b) Serration-1, (c) Serration-2, and (d) No-Cusp configurations.

1, and Serration-2 configurations at the angle of attack $\alpha = 18°$. Although the wavelet analysis was carried out for all the remote sensor locations, the spectrogram is presented only for pressure sensor M3 for brevity, since it demonstrated high levels of unsteady pressure loading in Fig. 13. For the Baseline case, the results show that the temporal characteristics of the signal exhibit amplitude modulation in time for the first three peaks seen in Fig. 11(b), signifying that the modes are amplitudes modulated over time. Additionally, the highest level of energy in the time-frequency domain is dominated by the peak at $St_s = 1.6$, corresponding to the vortex shedding frequency. Following that, Serration-1 portrays a similar trend, with a slight shift of the fundamental vortex shedding peak to a lower frequency region to $St_s = 1.5$, as seen earlier. As anticipated, in the case

of Serration-2 configuration, the wavelet coefficient modulus is well distributed over the frequency range with the absence of a peak or amplitude modulation. Furthermore, a fundamental peak with a much lower level of energy emerges in the contour for Serration-2 without the presence of other harmonic modes compared to the Baseline case. Contrary to the results seen in the case of Serration-1, the primary peak observed for the Serration-2 case occurs with a slight shift toward the higher frequency ($St_s = 2$), consistent with the results in Fig. 11(b). Additionally, the broadband hump demonstrates lower levels of energy with much lesser occurrences compared to the tones.

To further investigate the effect of amplitude modulation mechanics on the multiple tones generated by the high-lift device, the power spectral density (PSD) of the time signal and the wavelet coefficient modulus at selected frequencies are studied. The selected frequencies are the specific narrowband peaks (modes) observed in each configuration as shown in Figs. 11(b) and 20. The modes selected for the Baseline, Serration-1 and Serration-2 cases were St_{1-6}, St_{1-5} and St_{1-3}, respectively. Figure 23 shows the PSD of the wavelet coefficient magnitude ($E(St_s)$) in terms of slat chord-based Strouhal number (St_s) for the Baseline, Serration-1, and Serration-2 configurations at different selected frequencies. For remote sensor M3, the $E(St_s)$ for the Baseline case shows that for modes 4, 5, and 6, the amplitude is modulated by a frequency $\Delta St_{4,5,6} \approx 1.61$, i.e., the primary vortex shedding frequency. For mode 6, in addition to the modulation by the fundamental peak frequency, the amplitude is also moderately modulated by frequencies $\Delta St_6 \approx 3.2$ and 4.8. Interestingly, mode 3 is modulated by the the broadband spectral hump observed in Fig. 11(b) with a frequency $\Delta St_3 \approx 0.6 - 1$. For Serration-1, at modes 3, 4, and 5, the amplitude is modulated by a frequency $\Delta St_{3,4,5} \approx 1.61$, similar to the Baseline configuration. In the case of Serration-2, the results for all the modes (1-3) demonstrate that the amplitude of the wavelet coefficient magnitude is not modulated by any frequencies, consistent with the results observed in Figs. 20 and 21.

The stochastic analysis of the fluctuating characteristics of the surface pressure for various frequencies of interest was further analyzed using the arithmetic mean, standard deviation, and coefficient of variation of the wavelet coefficient modulus, i.e., $\mu(|W_x|)$, $\sigma(|W_x|)$, and CV($|W_x|$), respectively[57]. Stochastic analysis of the wavelet coefficient modulus at sensor location M3 for the Baseline, Serration-1, and Serration-2 configurations at angles of attack $\alpha = 18^\circ$ is presented in Fig. 24. The $\mu(|W_x|)$ for the Baseline and Serration-1 show increased fluctuations with similar values and trends at the vortex shedding frequency ($St_s = 1.6$), whereas, in the case of Serration-2, a significant reduction in $\mu(|W_x|)$ is observed. The $\sigma(|W_x|)$ indicates the level of distribution of

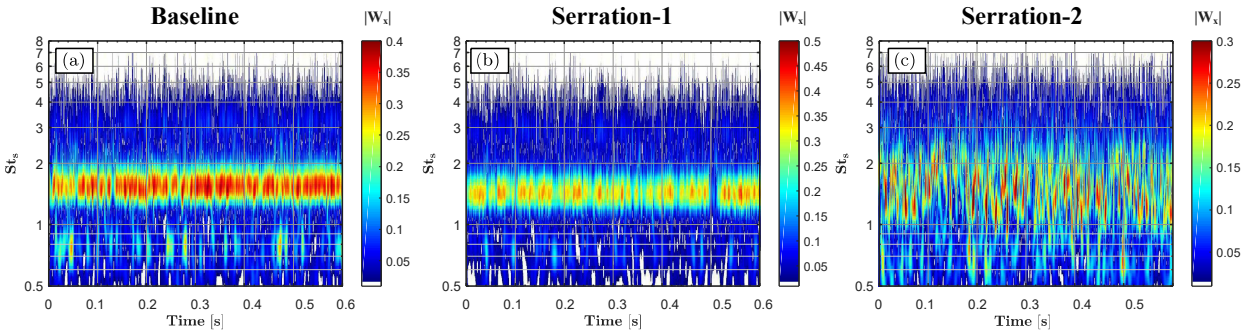

FIG. 22: Wavelet scalogram ($|W_x|$) for a segment of a pressure signal obtained at sensor location M3 at angle of attack $\alpha = 18°$ for (a) Baseline, (b) Serration-1, and (c) Serration-2 configurations.

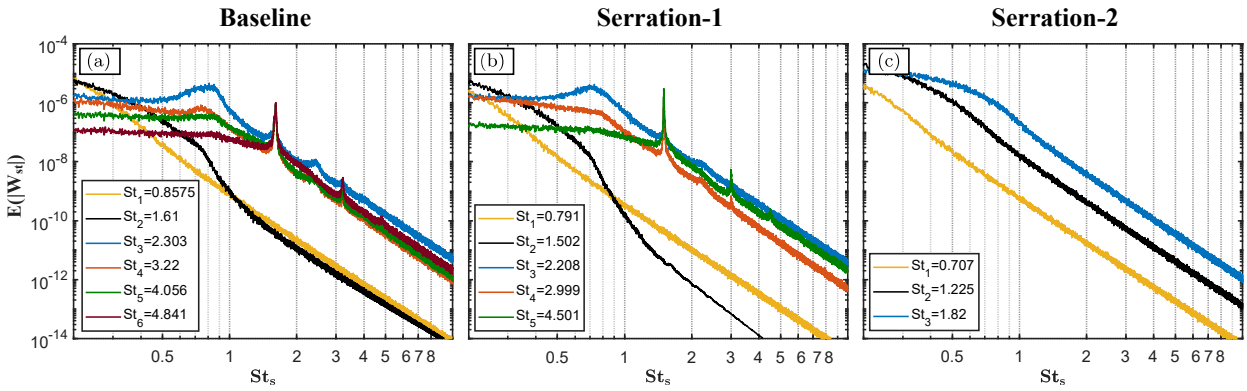

FIG. 23: Power spectral density the wavelet coefficient modulus at selected resonance frequencies at location M3 for angle of attack $\alpha = 18°$ for (a) Baseline, (b) Serration-1, and (c) Serration-2 configurations.

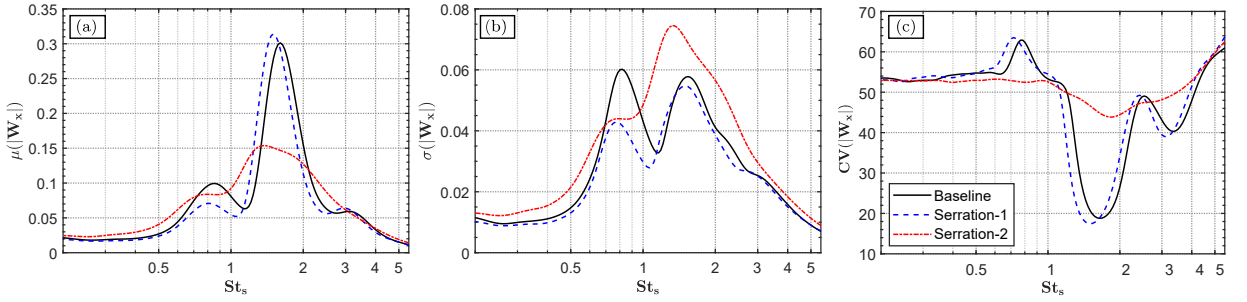

FIG. 24: Stochastic analysis of the wavelet coefficient modulus at location M3 for angle of attack $\alpha = 18°$: (a) arithmetic mean, (b) standard deviation and (c) coefficient of variation.

the pressure events from the mean at a given frequency. For Baseline and Serration-1, two notable peaks are observed in $\sigma(|W_x|)$ at $St_s = 0.8$ and $St_s = 1.6$, associated with the broadband hump

spectra and the fundamental vortex shedding frequency, respectively. Interestingly, for Serration-2, the $\sigma(|W_x|)$ exhibits a single wide hump with higher values than the Baseline and Serration-1, reaffirming the turbulent nature of the flow. The coefficient of variation CV($|W_x|$) is the ratio of the standard deviation to the mean which essentially shows the fluctuation intensity of the pressure signals at a given frequency in terms of percentage[58]. The higher the CV($|W_x|$), the greater the level of dispersion around the mean. The Baseline and Serration-1 exhibit the lowest CV($|W_x|$) at the vortex shedding frequency ($St_s = 1.6$) with just 17%, indicating the occurrence of a lower level of dispersion around the mean, i.e., lesser fluctuation intensity. Conversely, at $St_s = 0.8$, the CV($|W_x|$) for the Baseline and Serration-1 configuration indicate high values of about 64%, signifying the existence of a greater level of dispersion around the mean with higher fluctuation intensity. Interestingly, for Serration-2, the CV($|W_x|$) indicates marginal changes through the entire frequency range corresponding to the broadband nature of the flow. Furthermore, at the fundamental shedding frequency, the CV($|W_x|$) for the Serration-2 is considerably higher than that of the Baseline and Serration-1 cases, emphasizing the absence of characteristic slat flow features.

IV. CONCLUSION

This paper demonstrates the aerodynamic and aeroacoustic characteristics of a 30P30N three-element high-lift airfoil with and without the serrated slat cusp at angles of attack $\alpha = 14°$ and $18°$. Results were also provided for the No-Cusp configuration for the sake of comparison. The high-lift airfoil was highly equipped with static pressure taps and several surfaces mounted unsteady surface pressure measurement probes around the slat and the leading edge of the main-element region. Aerodynamic characteristics of the high-lift airfoil deduced from the distribution of the pressure coefficient remained unchanged with the application of the slat serrations. The near- and the far-field surface pressure measurements showed that the characteristic narrowband peaks from the slat noise could be eliminated with the application of Serration-2 for both the angles of attack compared to the Baseline and Serration-1. Moreover, the broadband hump observed in the Baseline was eliminated for the Serration-2 configuration. The auto-correlation results of the Serration-2 showed a very weak periodic shape with fast decaying periodic behavior compared to that of the Baseline case, implying that the application of Serration-2 could significantly suppress the development of vortex shedding. Additionally, the length-scale results for the Serration-2 case

show that the fundamental tonal peak could be noticeably reduced, although there is a slight shift in the spectral peak to the lower frequency range. The near-to the far-field coherence results showed a significant reduction of the broadband hump, the vortex shedding peak, and the other distinct narrowband peaks for the Serration-2 compared to the other tested configurations. The wavelet coefficient results demonstrated the spectral peaks for the Baseline case along with the amplitudes modulated in time, conversely, these peaks were absent in the case of Serration-2 configuration. The results also showed that the peaks observed in the Baseline case exhibit quadratic self-interaction in the slat cavity, whereas the constructive self-interaction of the modes could be weakened with the application Serration-2. Finally, this paper explicitly demonstrates that the application of Serration-2 significantly reduces the tonal peaks, and thus the noise generated by the slat cavity, altering the flow structures within the slat without adversely affecting the aerodynamic efficiency. This study has also shown that the use of serrations as a possibility for breaking the feedback mechanism that drives cavity based oscillations. However, further studies at higher Reynolds numbers are required to establish the noise reduction capabilities of serrated slat cusp for actual flight conditions.

DATA AVAILABILITY

The data that support the findings of this study are available from the corresponding author upon reasonable request.

REFERENCES

[1]H. Kamliya Jawahar, M. Azarpeyvand, R. Theunissen, and C. R. I. da Silva, "Aerodynamic and aeroacoustic performance of three-element high lift airfoil fitted with various cove fillers," in *2018 AIAA/CEAS Aeroacoustics Conference* (2018).

[2]H. Kamliya Jawahar, S. A. Showkat Ali, M. Azarpeyvand, and R. I. Carlos, "Aeroacoustic performance of threeelement high lift airfoil with slat cove fillers," in *25th AIAA/CEAS Aeroacoustic conference* (2019).

[3]H. Kamliya Jawahar, M. Azarpeyvand, and C. Ilario, "Experimental investigation of flow around three-element high-lift airfoil with morphing fillers," in *23rd AIAA/CEAS Aeroacoustics Conference* (2017) p. 3364.

[4]Q. Ai, H. Kamliya Jawahar, and M. Azarpeyvand, "Experimental investigation of aerodynamic performance of airfoils fitted with morphing trailing edges," in *54th AIAA aerospace sciences meeting* (2016) p. 1563.

[5]H. Kamliya Jawahar, Q. Ai, and M. Azarpeyvand, "Experimental and numerical investigation of aerodynamic performance of airfoils fitted with morphing trailing-edges," in *23rd AIAA/CEAS aeroacoustics conference* (2017) p. 3371.

[6]H. Kamliya Jawahar, Q. Ai, and M. Azarpeyvand, "Aerodynamic and aeroacoustic performance of airfoils fitted with morphing trailing-edges," in *2018 AIAA/CEAS Aeroacoustics Conference* (2018) p. 2815.

[7]H. Kamliya Jawahar, Q. Ai, and M. Azarpeyvand, "Experimental and numerical investigation of aerodynamic performance for airfoils with morphed trailing edges," Renewable Energy **127**, 355–367 (2018).

[8]S. A. Showkat Ali, M. Azarpeyvand, and C. R. I. da Silva, "Trailing-edge flow and noise control using porous treatments," Journal of Fluid Mechanics **850**, 83–119 (2018).

[9]S. A. Showkat Ali, M. Azarpeyvand, and C. R. I. da Silva, "Trailing edge bluntness noise reduction using porous treatments," Journal of Sound and Vibration **474**, 115257 (2020).

[10]S. A. Showkat Ali, M. Azarpeyvand, M. Szőke, and C. R. Ilário da Silva, "Boundary layer flow interaction with a permeable wall," Physics of Fluids **30**, 085111 (2018).

[11]S. A. Showkat Ali, M. Azarpeyvand, and C. R. I. da Silva, "Experimental study of porous treatment for aerodynamic and aeroacoustic purposes," in *23rd AIAA/CEAS Aeroacoustics Conference* (2017) p. 3358.

[12]A. Afshari, M. Azarpeyvand, A. A. Dehghan, M. Szoke, and R. Maryami, "Trailing-edge flow manipulation using streamwise finlets," Journal of Fluid Mechanics **870**, 617–650 (2019).

[13]X. Liu, H. Kamliya Jawahar, M. Azarpeyvand, and R. Theunissen, "Aerodynamic performance and wake development of airfoils with serrated trailing-edges," AIAA Journal **55**, 3669–3680 (2017).

[14]Y. D. Mayer, B. Lyu, H. K. Jawahar, and M. Azarpeyvand, "A semi-analytical noise prediction model for airfoils with serrated trailing edges," Renewable Energy **143**, 679–691 (2019).

[15]S. S. Vemuri, X. Liu, B. Zang, and M. Azarpeyvand, "On the use of leading-edge serrations for noise control in a tandem airfoil configuration," Physics of Fluids **32**, 077102 (2020).

[16]M. Szőke, D. Fiscaletti, and M. Azarpeyvand, "Uniform flow injection into a turbulent boundary layer for trailing edge noise reduction," Physics of Fluids **32**, 085104 (2020).

[17]M. Szőke, D. Fiscaletti, and M. Azarpeyvand, "Effect of inclined transverse jets on trailing-edge noise generation," Physics of Fluids **30**, 085110 (2018).

[18]M. Roger and S. Perennes, "Low-frequency noise sources in two-dimensional high-lift devices," in *6th Aeroacoustics Conference and Exhibit* (2000) p. 1972.

[19]A. Kolb, P. Faulhaber, R. Drobietz, and M. Grünewald, "Aeroacoustic wind tunnel measurements on a 2d high-lift configuration," in *13th AIAA/CEAS Aeroacoustics Conference* (2007) p. 3447.

[20]J. Mendoza, T. Brooks, and W. Humphreys Jr, "An aeroacoustic study of a leading edge slat configuration," International Journal of Aeroacoustics **1**, 241–274 (2002).

[21]S. Hein, T. Hohage, W. Koch, and J. Schöberl, "Acoustic resonances in a high-lift configuration," Journal of Fluid Mechanics **582**, 179–202 (2007).

[22]M. Murayama, K. Nakakita, K. Yamamoto, H. Ura, Y. Ito, and M. M. Choudhari, "Experimental study on slat noise from 30p30n three-element high-lift airfoil at jaxa hard-wall lowspeed wind tunnel," in *20th AIAA/CEAS Aeroacoustics Conference* (2014) p. 2080.

[23]M. Terracol, E. Manoha, and B. Lemoine, "Investigation of the unsteady flow and noise generation in a slat cove," AIAA Journal **54**, 469–489 (2016).

[24]C. C. Pagani Jr, D. S. Souza, and M. A. Medeiros, "Slat noise: aeroacoustic beamforming in closed-section wind tunnel with numerical comparison," AIAA Journal **54**, 2100–2115 (2016).

[25]C. C. Pagani, D. S. Souza, and M. A. Medeiros, "Experimental investigation on the effect of slat geometrical configurations on aerodynamic noise," Journal of Sound and Vibration **394**, 256–279 (2017).

[26]K. A. Pascioni and L. N. Cattafesta, "Unsteady characteristics of a slat-cove flow field," Physical Review Fluids **3**, 034607 (2018).

[27]L. Li, P. Liu, H. Guo, Y. Hou, X. Geng, and J. Wang, "Aeroacoustic measurement of 30p30n high-lift configuration in the test section with kevlar cloth and perforated plate," Aerospace Science and Technology **70**, 590–599 (2017).

[28]L. Li, P. Liu, H. Guo, X. Geng, Y. Hou, and J. Wang, "Aerodynamic and aeroacoustic experimental investigation of 30p30n high-lift configuration," Applied Acoustics **132**, 43–48 (2018).

[29]L. Li, P. Liu, Y. Xing, and H. Guo, "Time-frequency analysis of acoustic signals from a high-lift configuration with two wavelet functions," Applied Acoustics **129**, 155–160 (2018).

[30]L. Li, P. Liu, Y. Xing, and H. Guo, "Wavelet analysis of the far-field sound pressure signals generated from a high-lift configuration," AIAA Journal **56**, 432–437 (2018).

[31]Y. Li, X. Wang, and D. Zhang, "Control strategies for aircraft airframe noise reduction," Chinese Journal of Aeronautics **26**, 249–260 (2013).

[32]W. Dobrzynski, B. Gehlhar, and H. Buchholz, "Model and full scale high-lift wing wind tunnel experiments dedicated to airframe noise reduction," Aerospace science and technology **5**, 27–33 (2001).

[33]M. R. Khorrami and D. P. Lockard, "Effects of geometric details on slat noise generation and propagation," International Journal of aeroacoustics **9**, 655–678 (2010).

[34]W. Horne, K. James, T. Arledge, P. Soderman, N. Burnside, and S. Jaeger, "Measurements of 26%-scale 777 airframe noise in the nasa ames 40-by 80 foot wind tunnel," in *11th AIAA/CEAS Aeroacoustics Conference* (2005) p. 2810.

[35]H. Kamliya Jawahar, R. Theunissen, M. Azarpeyvand, and C. R. I. da Silva, "Flow characteristics of slat cove fillers," Aerospace Science and Technology **100**, 105789 (2020).

[36]H. Kamliya Jawahar, S. A. Showkat Ali, M. Azarpeyvand, and C. R. I. da Silva, "Aerodynamic and aeroacoustic performance of high-lift airfoil fitted with slat cove fillers," Journal of Sound and Vibration **479**, 115347 (2020).

[37]T. L. Turner and D. L. Long, "Development of a sma-based, slat-gap filler for airframe noise reduction," in *23rd AIAA/AHS Adaptive Structures Conference* (2015) p. 0730.

[38]Z. Ma, M. Smith, S. Richards, and X. Zhang, "Slat noise attenuation using acoustic liner," in *11th AIAA/CEAS Aeroacoustics Conference* (2005) p. 3009.

[39]W. Dobrzynski, K. Nagakura, B. Gehlhar, and A. Buschbaum, "Airframe noise studies on wings with deployed high-lift devices," in *4th AIAA/CEAS Aeroacoustics Conference* (1998) p. 2337.

[40]V. Kopiev, M. Zaitsev, I. Belyaev, and M. Mironov, "Noise reduction potential through slat hook serrations," in *17th AIAA/CEAS Aeroacoustics Conference (32nd AIAA Aeroacoustics Conference)* (2011) p. 2909.

[41]W. Dobrzynski, H. Bieler, L. Chow, and H. Remy, "The airframe noise reduction challenge: lessons learned from the european silencer project," in *Proposed Paper for DGLR Conference" Deutscher Luft und Raumfahrt Kongress" in Braunschweig* (2006).

[42]M. Herr, "A noise reduction study on flow-permeable trailing-edges," CD Proceedings ODAS 2007 (2007).

[43]C. Streett, J. Casper, D. Lockard, M. Khorrami, R. Stoker, R. Elkoby, W. Wenneman, J. Underbrink, W. Wenneman, and J. Underbrink, "Aerodynamic noise reduction for high-lift devices on a swept wing model," in *44th AIAA Aerospace Sciences Meeting and Exhibit* (2006) p. 212.

[44]C. Andreou, W. Graham, and H.-C. Shin, "Aeroacoustic study of airfoil leading edge high-lift devices," in *12th AIAA/CEAS Aeroacoustics Conference* (2006) p. 2515.

[45]C. Andreou, W. Graham, and H.-C. Shin, "Aeroacoustic comparison of airfoil leading edge high-lift geometries and supports," in *45th AIAA Aerospace Sciences Meeting and Exhibit* (2007) p. 230.

[46]T. Imamura, H. Ura, Y. Yokokawa, S. Enomoto, K. Yamamoto, and T. Hirai, "Designing of slat cove filler as a noise reduction device for leading-edge slat," in *13th AIAA/CEAS Aeroacoustics Conference* (2007) p. 3473.

[47]H. Ura, Y. Yokokawa, T. Imamura, T. Ito, and K. Yamamoto, "Investigation of airframe noise from high lift configuration model," in *46th AIAA Aerospace Sciences Meeting and Exhibit* (2008) p. 19.

[48]A. Shmilovich, Y. Yadlin, and D. M. Pitera, "Wing leading edge concepts for noise reduction," in *27th International Congress of the Aeronautical Sciences* (2010).

[49]A. Shmilovich, Y. Yadlin, *et al.*, "High-lift systems for enhanced takeoff performance," in *28th International Congress of the Aeronautical Sciences* (2012).

[50]W. D. Scholten, D. J. Hartl, T. L. Turner, and R. T. Kidd, "Development and analysis-driven optimization of superelastic slat-cove fillers for airframe noise reduction," AIAA Journal **54**, 1078–1094 (2016).

[51]J. Tao and G. Sun, "A novel optimization method for maintaining aerodynamic performances in noise reduction design," Aerospace Science and Technology **43**, 415–422 (2015).

[52]Y. D. Mayer, H. K. Jawahar, M. Szőke, S. A. S. Ali, and M. Azarpeyvand, "Design and performance of an aeroacoustic wind tunnel facility at the university of bristol," Applied Acoustics **155**, 358–370 (2019).

[53]E. Manoha and M. Pott-Pollenske, "Leisa2: an experimental database for the validation of numerical predictions of slat unsteady flow and noise," in *21st AIAA/CEAS Aeroacoustics Conference* (2015) p. 3137.

[54]M. Farge, "Wavelet transforms and their applications to turbulence," Annual Review of Fluid Mechanics **24**, 395–458 (1992).

[55]S. Mallat, *A wavelet tour of signal processing* (Elsevier, 1999).

[56]J. Morlet, "Sampling theory and wave propagation," in *Issues in acoustic Signal-image processing and recognition* (Springer, 1983) pp. 233–261.

[57]H. Kamliya Jawahar, M. Azarpeyvand, and C. R. I. da Silva, "Acoustic and flow characteristics of an airfoil fitted with morphed trailing edges," Experimental Thermal and Fluid Science , 110287 (2020).

[58]P. S. Addison, *The illustrated wavelet transform handbook: introductory theory and applications in science, engineering, medicine and finance* (CRC press, 2017).